aerospace

MDPI

Article

Numerical Investigation of the Effect of Circumferentially Non-Uniform Injection on the Propagation Direction of MMH/NTO Rotating Detonation in a Hollow Combustor

Yunhao Xiong [1], Wei Lin [1,2,*], Kangkang Guo [1], Yihang Qin [1], Xiaoliang Li [1] and Qiaofeng Xie [3]

[1] Department of Aerospace Science and Technology, Space Engineering University, Beijing 101416, China; xiongyunhao@hgd.edu.cn (Y.X.)
[2] Innovation Center for Space Launch Testing and TT&C Technology, Space Engineering University, Beijing 101416, China
[3] Institute for Aero Engine, Tsinghua University, Beijing 100084, China
* Correspondence: linweiqy@163.com

Abstract

The uncertain propagation direction of rotating detonation in hollow combustors limits the predictability of liquid hypergolic propulsion systems. In this study, the effect of circumferentially non-uniform injection on the propagation direction of monomethylhydrazine/nitrogen tetroxide (MMH/NTO) rotating detonation is numerically investigated. Different injection-intensity distributions are established by varying the local mass flow rate and injection velocity while maintaining the total propellant mass flow rate and overall oxidizer-to-fuel ratio. The results show that configurations with shorter injector groups exhibit inconsistent propagation directions, whereas the S_4–M_4–L_4 configuration at a non-uniformity amplitude of 0.4 shows a clear directional preference consistent with the injection arrangement. At $\delta = 0.6$, opposite-direction propagation was observed in limited simulations, indicating a non-monotonic directional response under the investigated conditions. Reversing the injection arrangement after stable rotating detonation is established does not reverse the propagation direction. Transient pressure fields further reveal competition between oppositely propagating circumferential pressure waves during detonation establishment. These results indicate that circumferentially non-uniform injection mainly influences propagation-direction selection during the establishment stage.

Keywords: MMH/NTO; rotating detonation; hollow combustor; circumferentially non-uniform injection; propagation direction; numerical simulation

Check for updates

Academic Editor: Jae Hyun Park

Received: 19 August 2026
Revised: 30 September 2026
Accepted: 1 October 2026
Published: 4 October 2026

Copyright: © 2026 by the authors. Licensee MDPI, Basel, Switzerland. This article is an open access article distributed under the terms and conditions of the Creative Commons Attribution (CC BY) license.

1. Introduction

A rotating detonation engine (RDE) sustains one or more detonation waves that continuously propagate in the circumferential direction within the combustor, enabling periodic propellant replenishment and rapid heat release. Owing to its compact configuration, potential for pressure gain, and high thermodynamic efficiency, the RDE has been regarded as a promising propulsion concept for aerospace applications. In recent years, increasing attention has been directed toward liquid-propellant rotating detonation for space propulsion applications [1,2]. Unlike conventional predominantly axial combustion, rotating detonation inherently induces pronounced circumferential flow and may consequently generate torque about the engine axis [3]. Sawada et al. [4] experimentally measured the axial torque produced by an RDE and found that the torque direction changed with the

propagation direction of the detonation wave. Goto et al. [5] further demonstrated an RDE in space using a sounding rocket and observed an increase in the vehicle roll rate during engine operation, while a pulse detonation engine was incorporated into the same flight system to regulate the rotational motion [6]. These findings indicate that, for propulsion systems intended for spacecraft attitude and orbit control, the magnitude and direction of RDE-induced torque should be sufficiently predictable. Otherwise, random selection between clockwise (CW) and counterclockwise (CCW) detonation propagation may introduce additional disturbances into spacecraft attitude-control systems.

Control of the rotating-detonation propagation direction has been investigated through initiation control, asymmetric combustor configurations, and propellant-injection strategies. Early studies employed barriers or controlled initiation to suppress propagation in the undesired direction [7]. Boening et al. [8] used circumferentially distributed wave generators fired according to a prescribed phase sequence, whereas Sheng et al. [9] employed a predetonator as an active control device during operation. Configuration-based approaches subsequently introduced geometric asymmetries such as steps, guide vanes, Tesla-valve-type channels, and helical combustors [10–14]. Sawada et al. [14], for example, obtained a propagation direction consistent with the handedness of a helical combustor, although the asymmetric geometry itself also generated additional torque. More recently, propagation-direction control has been extended to propellant-injection strategies. Injector configurations and inlet conditions have been shown to substantially affect rotating-detonation establishment and propagation characteristics [15,16]. Braun et al. [17] investigated swirl injection as a means of promoting preferential propagation, whereas Yamamoto et al. [18] directly introduced circumferential momentum through tangential swirl injection and obtained propagation in the positive-swirl direction in all 22 tests. Although these approaches can provide directional control, they generally require additional initiation devices, geometric asymmetry, or deliberately imposed circumferential momentum.

Monomethylhydrazine/nitrogen tetroxide (MMH/NTO) is a representative liquid bipropellant combination for spacecraft attitude- and orbit-control propulsion systems [19,20]. Because MMH and NTO ignite spontaneously upon contact, the establishment of rotating detonation involves strongly coupled processes of droplet transport, evaporation, mixing, hypergolic reaction, and transient pressure-wave interaction, making direction-control approaches based solely on external ignition timing difficult to apply directly. Experimental and numerical investigations by Gu et al. [21–23] showed that self-sustained MMH/NTO rotating detonation can establish spontaneously in an annular combustor and may undergo a low-amplitude unstable stage before stable propagation is achieved. However, most existing studies of MMH/NTO rotating detonation have focused on annular combustors [24–31]. In comparison, a hollow combustor eliminates the centerbody and thereby alleviates the associated structural and thermal-protection constraints [32]. At the same time, removal of the centerbody modifies shock reflection, the central flow field, and the organization of circumferential wave structures, potentially leading to establishment dynamics that differ from those in annular configurations [33–39]. Our previous numerical studies [40–43] demonstrated the feasibility of establishing and sustaining MMH/NTO rotating detonation in a hollow combustor; however, the mechanism governing the selection of the propagation direction remains unclear.

Studies of tangential combustion instability in hollow liquid rocket combustors provide useful mechanistic insights into the formation and competition of circumferential wave systems. Sung et al. [44] numerically showed that CW- and CCW-propagating pressure waves can coexist during the early development of self-excited tangential instability, after which one propagation direction gradually becomes dominant as the two wave systems evolve asymmetrically. Guo et al. [45] further showed that modifying only the local fuel

mass flow rate could induce strong first-order tangential instability in a liquid oxygen (LOX)/kerosene combustor, demonstrating that local propellant supply can substantially alter the coupling between circumferential pressure waves and unsteady heat release. These findings suggest that, in a hollow combustor, the ultimately dominant circumferential propagation direction may emerge through competition between oppositely propagating wave systems, while the outcome of this competition may itself be modulated by local propellant-supply conditions.

Based on these considerations, the present study investigates the effect of circumferentially non-uniform injection on the propagation-direction selection of MMH/NTO rotating detonation in a hollow combustor. Unlike initiation-timing-based approaches, the proposed strategy does not require an independent ignition device; unlike asymmetric-combustor approaches, it does not modify the main combustor geometry; and unlike swirl-injection approaches, it does not directly impose circumferential momentum. Instead, the local mass flow rate and initial injection velocity are varied circumferentially while the total propellant mass flow rate and overall oxidizer-to-fuel ratio are maintained constant. Propellant-supply distributions with different non-uniformity amplitudes, circumferential injector-group lengths, and arrangement directions are examined to evaluate their effects on propagation-direction selection. In addition, reversal of the injection arrangement after stable rotating detonation has been established, together with the transient evolution of the pressure field during the establishment stage, is analyzed to clarify how circumferential redistribution of the propellant supply influences propagation-direction selection and subsequent stable propagation.

2. Numerical Model and Computational Methods

2.1. Governing Equations and Numerical Methods

A three-dimensional unsteady numerical model of an MMH/NTO rotating-detonation hollow combustor was established using the commercial computational fluid dynamics (CFD) software ANSYS Fluent 2020 R2.

The continuous gas phase is governed by the compressible conservation equations of mass, momentum, total energy, and chemical species. With source terms introduced to account for the two-way coupling with the discrete droplet phase, the equations are written as

$$\frac{\partial \rho}{\partial t} + \nabla \cdot (\rho \mathbf{u}) = S_m^{(d)}, \tag{1}$$

$$\frac{\partial (\rho \mathbf{u})}{\partial t} + \nabla \cdot (\rho \mathbf{u}\mathbf{u}) = -\nabla p + \nabla \cdot \boldsymbol{\tau} + \mathbf{S}_{\mathrm{mom}}^{(d)}, \tag{2}$$

$$\frac{\partial (\rho E)}{\partial t} + \nabla \cdot [(\rho E + p)\mathbf{u}] = \nabla \cdot (\boldsymbol{\tau} \cdot \mathbf{u} - \mathbf{q}) + S_E^{(d)} + S_E^{(r)}, \tag{3}$$

$$\frac{\partial (\rho Y_k)}{\partial t} + \nabla \cdot (\rho \mathbf{u} Y_k) = -\nabla \cdot \mathbf{J}_k + \dot{\omega}_k + S_k^{(d)}, \qquad k = 1, \ldots, N_s. \tag{4}$$

Here, ρ, $\mathbf{u}$, p, and E denote the gas density, velocity, pressure, and specific total energy, respectively; Y_k is the mass fraction of species k; $\dot{\omega}_k$ is its chemical-production rate; and $S_m^{(d)}$, $\mathbf{S}_{\mathrm{mom}}^{(d)}$, $S_E^{(d)}$, and $S_k^{(d)}$ are the interphase mass, momentum, energy, and species source terms generated by droplet evaporation and gas–liquid coupling. $S_E^{(r)}$ denotes the energy source associated with chemical reaction. The specific total energy is $E = e + \mathbf{u} \cdot \mathbf{u}/2$. The viscous stress tensor and heat flux are expressed as

$$\boldsymbol{\tau} = \mu\left[\nabla\mathbf{u} + (\nabla\mathbf{u})^T - \frac{2}{3}(\nabla\cdot\mathbf{u})\mathbf{I}\right], \tag{5}$$

$$\mathbf{q} = -\lambda\nabla T + \sum_{k=1}^{N_s} h_k\mathbf{J}_k, \qquad \mathbf{J}_k = -\rho D_k\nabla Y_k, \tag{6}$$

where μ and λ are the dynamic viscosity and thermal conductivity, respectively, h_k is the specific enthalpy of species k, and D_k is its mass-diffusion coefficient. The gas mixture is treated as an ideal gas:

$$p = \rho R_{\mathrm{mix}} T, \qquad R_{\mathrm{mix}} = R_u \sum_{k=1}^{N_s} \frac{Y_k}{M_k}, \tag{7}$$

where R_u is the universal gas constant, and M_k is the molar mass of species k.

The liquid propellants were modeled using the discrete phase model (DPM). The post-primary-atomization spray was represented by discrete MMH and NTO droplets introduced at the nominal impingement locations, while the primary liquid–liquid impinging-jet atomization process was not explicitly resolved. The translational motion of an individual droplet is described in a Lagrangian framework as

$$\frac{d\mathbf{u}_p}{dt} = \mathbf{F}_D(\mathbf{u} - \mathbf{u}_p) + \frac{\rho_p - \rho}{\rho_p}\mathbf{g} + \mathbf{F}_{\mathrm{pg}} + \mathbf{F}_{\mathrm{th}}, \tag{8}$$

where $\mathbf{u}_p$ and ρ_p are the droplet velocity and density, respectively, $\mathbf{F}_D$ denotes the drag contribution per unit droplet mass, and $\mathbf{F}_{\mathrm{pg}}$ and $\mathbf{F}_{\mathrm{th}}$ are the pressure-gradient and thermophoretic-force contributions. Droplet collision and secondary breakup of the prescribed droplets were not explicitly modeled. These processes may affect the quantitative droplet-size evolution, evaporation rate, and the resulting local vapor and heat-release distributions. The same prescribed Rosin–Rammler droplet distributions and spray-modeling parameters were used for all comparative cases.

Droplet evaporation was described using a convection/diffusion-controlled model. Defining the evaporation rate $\dot{m}_{\mathrm{vap}} = -dm_p/dt > 0$, the droplet mass and temperature evolve according to

$$\frac{dm_p}{dt} = -\dot{m}_{\mathrm{vap}}, \tag{9}$$

$$m_p c_{p,p}\frac{dT_p}{dt} = hA_p(T - T_p) - \dot{m}_{\mathrm{vap}} h_{fg}, \tag{10}$$

where m_p, T_p, $c_{p,p}$, and A_p are the droplet mass, temperature, specific heat, and surface area, respectively; h is the convective heat-transfer coefficient, and h_{fg} is the latent heat of vaporization. The local mass-transfer rate is evaluated from the convection/diffusion formulation using the Spalding mass-transfer number:

$$B_M = \frac{Y_{v,s} - Y_{v,\infty}}{1 - Y_{v,s}}, \tag{11}$$

where $Y_{v,s}$ and $Y_{v,\infty}$ denote the vapor mass fractions at the droplet surface and in the surrounding gas, respectively. The vaporized MMH and NTO are added to the corresponding gas-phase species equations through $S_k^{(d)}$, while the associated mass, momentum, and energy exchanges contribute to $S_m^{(d)}$, $\mathbf{S}_{\mathrm{mom}}^{(d)}$, and $S_E^{(d)}$, respectively.

Two-way interaction between the continuous and discrete phases was enabled. Unsteady particle tracking was synchronized with the continuous-phase time step, the DPM

source terms were updated every flow iteration, and the DPM iteration interval was set to 20. These settings were kept unchanged for all comparative simulations.

Turbulence was modeled using the Stress-Blended Eddy Simulation (SBES) approach based on the shear-stress transport (SST) k–ω model. The Reynolds-averaged Navier–Stokes (RANS) formulation was applied in the near-wall region, whereas the large-eddy simulation (LES) formulation was employed in the scale-resolving region. The unresolved turbulent scales were modeled using the Wall-Adapting Local Eddy-Viscosity (WALE) subgrid-scale model.

The gas-phase hypergolic reaction of MMH/NTO was represented using the two-step, nine-species global reaction mechanism actually implemented in the present simulations. The two global reactions are

$$CH_6N_2 + 0.825\,N_2O_4 \rightarrow 0.7\,CO + 0.3\,CO_2 + H_2 + 2\,H_2O + 1.825\,N_2, \quad (12)$$

$$H_2O \rightarrow OH + H. \quad (13)$$

Both reactions were implemented as irreversible volumetric reactions. For reaction r, the finite-rate kinetic coefficient was evaluated in Arrhenius form:

$$k_r = A_r T^{\beta_r} \exp\left(-\frac{E_{a,r}}{R_u T}\right), \quad (14)$$

and the corresponding finite-rate reaction rate was evaluated from the prescribed reactant rate exponents:

$$R_r = k_r \prod_j C_j^{\eta_{j,r}}, \quad (15)$$

where A_r is the pre-exponential factor, β_r is the temperature exponent, $E_{a,r}$ is the activation energy, R_u is the universal gas constant, C_j is the molar concentration of reactant j, and $\eta_{j,r}$ is its rate exponent. The kinetic parameters used in the simulations are summarized in Table 1.

Table 1. Two-step global monomethylhydrazine/nitrogen tetroxide (MMH/NTO) reaction mechanism and kinetic parameters used in the simulations.

Reaction	Global Reaction	A_r	$E_{a,r}$ (J/kgmol)	β_r	Reactant Rate Exponents
R1	$CH_6N_2 + 0.825\,N_2O_4 \rightarrow 0.7\,CO + 0.3\,CO_2 + H_2 + 2\,H_2O + 1.825\,N_2$	1.2×10^7	2	0	$\eta_{MMH} = 1$, $\eta_{N_2O_4} = 0.825$
R2	$H_2O \rightarrow OH + H$	3.5×10^9	4.3984×10^8	0	$\eta_{H_2O} = 1$

For R1, for which its overall reaction order is 1.825, the pre-exponential factor has units of $(m^3/kgmol)^{0.825}\,s^{-1}$; for the first-order R2 reaction, the unit of A_r is s^{-1}. The first global reaction is therefore formulated as a kinetically fast overall MMH/NTO reaction within the present reduced model, whereas the second reaction provides the high-temperature dissociation pathway from H_2O to OH and H.

Turbulence–chemistry interaction was treated using the Finite-Rate/Eddy-Dissipation (FR/ED) model. In this formulation, the local reaction rate is limited by the smaller Arrhenius finite-rate value and the turbulent-mixing-controlled eddy-dissipation value. The mixing-rate constants used in the present simulations were $A_{mix} = 4.0$ and $B_{mix} = 0.5$. Thus, the two-step mechanism should be interpreted as a reduced global chemistry model coupled with turbulent mixing, rather than as a detailed elementary-kinetics mechanism.

For spatial discretization, the pressure term was discretized using a second-order scheme, while a bounded central-differencing scheme was employed for the momentum equations. The turbulent kinetic energy and species-transport equations were discretized

using a second-order upwind scheme. Pressure–velocity coupling was achieved using the Pressure-Implicit with Splitting of Operators (PISO) algorithm, and the transient terms were discretized using a second-order implicit scheme. The time step was determined according to the Courant–Friedrichs–Lewy (CFL) condition to ensure the stability and accuracy of the unsteady rotating-detonation simulations.

Before applying the numerical model to the hollow combustor, a previously published experiment on MMH/NTO rotating detonation in an annular combustor [26] was selected for validation to assess the capability of the model to reproduce the principal propagation characteristics of liquid hypergolic rotating detonation. Because publicly available experimental data for an MMH/NTO hollow combustor corresponding directly to the configuration considered in the present study are currently unavailable, an annular-combustor experiment using the same propellant combination and comparable injection conditions was employed for comparison. The numerical model was evaluated by comparing characteristic parameters, including the pressure history, dominant pressure frequency, and detonation-wave propagation velocity.

The validation therefore focuses on these experimentally measurable macroscopic characteristics; detailed internal transient flow fields are not directly accessible from the available experimental data.

Accordingly, the annular-combustor validation is used to establish the model's capability for these measurable propagation characteristics, while the hollow-combustor simulations are used to examine the relative effects of circumferential injection redistribution on rotating-detonation establishment and propagation-direction selection under the present configuration and operating conditions.

The MMH/NTO annular rotating-detonation experiment conducted by Yan et al. [26] was selected as the validation case. The experimental combustor had inner and outer diameters of 30 and 60 mm, respectively, and employed 24 pairs of liquid–liquid impinging injectors. The oxidizer and fuel orifice diameters were 0.4 and 0.3 mm, respectively. For the rotating-detonation condition used for comparison, the oxidizer and fuel mass flow rates were 150 and 90 g/s, respectively, corresponding to an oxidizer-to-fuel mass ratio of approximately 1.67. A numerical model corresponding to these experimental conditions was established, and the pressure signal at monitoring point P8, corresponding to the measurement location used in the experiment, was extracted for comparison.

The validation computation employed approximately 0.60 million cells and a time step of 8×10^{-7} s. The pressure-history characteristics, dominant pressure frequency, and detonation-wave propagation velocity were used as the principal validation criteria because these quantities were directly available from the reference experiment.

The experiment reported a dominant pressure frequency of approximately 7340 Hz and an average detonation-wave propagation velocity of approximately 1384 m/s, with instantaneous values ranging from 1208 to 1625 m/s. The measured detonation pressure peaks were typically approximately 0.4 MPa during the stable stage, with a maximum value of approximately 0.6 MPa [26].

Figure 1 presents the numerically obtained pressure history at monitoring point P8. During stable propagation, the pressure signal exhibits pronounced periodic spike-like oscillations, characterized by a rapid pressure rise followed by gradual decay. This behavior is consistent with the experimentally observed pressure fluctuations produced by the periodic passage of the rotating detonation wave over the monitoring location. The calculated peak pressure is approximately 0.38–0.41 MPa, whereas the minimum pressure is approximately 0.09–0.10 MPa. The calculated peak-pressure level is therefore close to the approximately 0.4 MPa pressure peaks reported during the stable experimental stage while remaining below the maximum experimental peak of approximately 0.6 MPa [26].

This agreement indicates that the numerical model reasonably reproduces the characteristic pressure-oscillation level of liquid hypergolic rotating detonation.

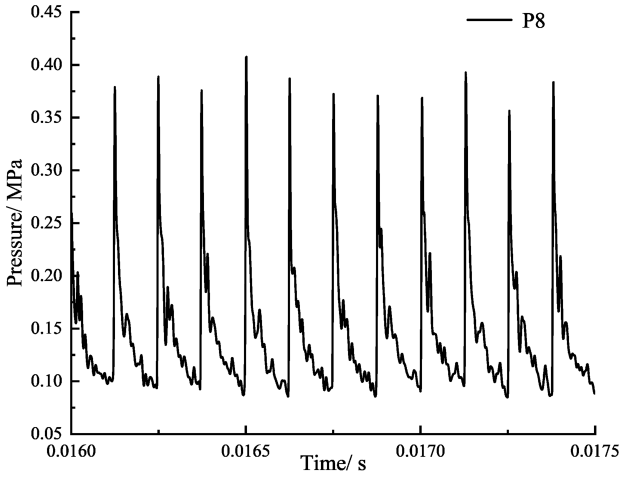


Figure 1. Pressure signal at P8 in the annular combustor.

To further evaluate the capability of the numerical model to predict the detonation propagation frequency, fast Fourier transform (FFT) analysis was performed on the pressure signal during the stable propagation stage, as shown in Figure 2. The calculated dominant pressure frequency is 7784 Hz, corresponding to a relative deviation of approximately 6.0% from the experimental value of 7340 Hz [26]. Overall, the numerical results reproduce the principal periodic characteristics of the rotating-detonation pressure signal observed experimentally. It should be noted that part of the frequency discrepancy may arise from the different pressure-signal intervals used for the frequency-domain analysis: the complete pressure history was subjected to FFT analysis in the experimental study [26], whereas only the stable rotating-detonation stage was analyzed in the present simulation.

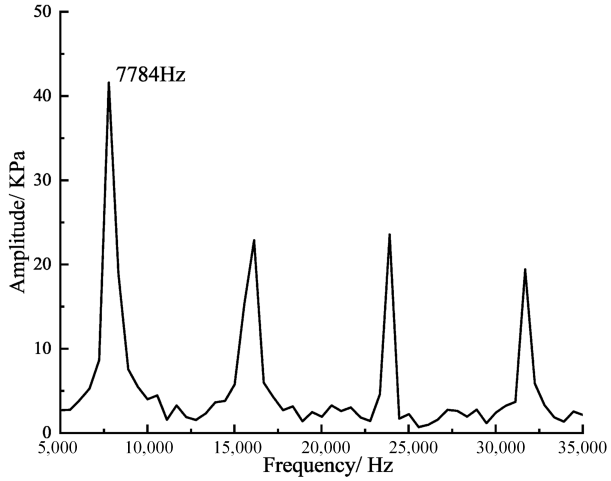


Figure 2. Fast Fourier transform (FFT) spectrum of the pressure signal at P8.

Based on the dominant pressure frequency, the circumferential propagation velocity of the detonation wave was calculated to be approximately 1467 m/s. This value differs by approximately 6.0% from the experimentally reported average velocity of 1384 m/s and lies within the measured range of 1208–1625 m/s [26]. This agreement further demonstrates the capability of the numerical model to predict the principal propagation characteristics of liquid hypergolic rotating detonation.

Taken together, the comparisons of the pressure history, dominant frequency, and detonation-wave propagation velocity indicate that the present multiphase reacting-flow framework, including droplet transport and evaporation, the two-step global reaction mechanism, and the FR/ED turbulence–chemistry treatment, can reasonably reproduce the major measurable propagation characteristics of liquid hypergolic rotating detonation. The model is therefore adopted for the subsequent investigation of the effects of circumferentially non-uniform injection on MMH/NTO rotating detonation in a hollow combustor.

2.2. Computational Domain, Boundary Conditions, and Injection Conditions

The configuration considered in this study is an MMH/NTO hypergolic rotating-detonation hollow combustor. The computational domain is consistent with that employed in our previous study to ensure comparability among the different cases. The hollow combustor has an inner diameter of 84 mm and an axial length of 150 mm. At the combustor head end, 48 pairs of liquid–liquid impinging injection locations are uniformly distributed along a circle with a diameter of 70 mm. Each injection location contains one discrete-phase inlet for MMH and one for NTO, resulting in a total of 96 DPM injection inlets. Liquid MMH and NTO enter the combustor as discrete droplets and subsequently undergo droplet transport, evaporation, gas–liquid mixing, and hypergolic reaction. The computational domain and the location of the pressure monitoring point are shown in Figure 3.

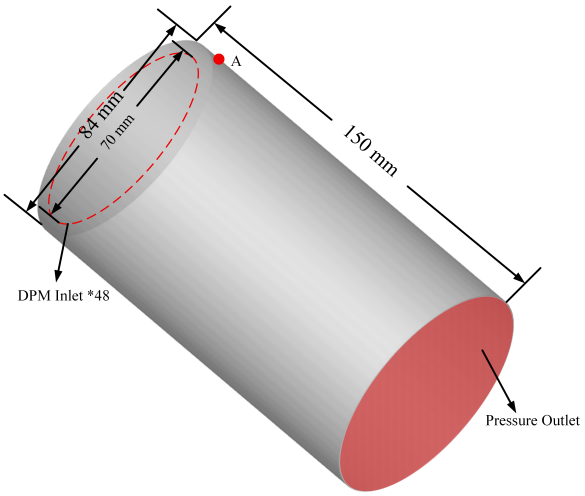


Figure 3. Schematic of the computational domain and pressure monitoring point A. DPM denotes the discrete phase model; the asterisk (*) in "DPM Inlet *48" denotes multiplication and indicates 48 pairs of impinging injection locations.

All solid surfaces of the combustor, including the head-end surface outside the discrete-phase injection locations, were treated as stationary no-slip adiabatic walls, i.e., $\mathbf{u} = 0$ and $\mathbf{n} \cdot \nabla T = 0$. A pressure-outlet boundary condition was imposed at the physical combustor exit, with the outlet static pressure prescribed as $p_{\text{out}} = 101{,}325$ Pa (1 atm). No continuous-phase mass-flow inlet was imposed at the head end; MMH and NTO were supplied exclusively through the DPM injection locations. The principal boundary and injection conditions are summarized in Table 2.

Table 2. Boundary and injection conditions used for the hollow-combustor simulations.

Boundary/Injection	Type	Condition
Combustor walls	Wall	Stationary, no-slip, adiabatic: $\mathbf{u} = 0$, $\mathbf{n} \cdot \nabla T = 0$
Combustor exit	Pressure outlet	Static pressure $p_{\text{out}} = 101{,}325$ Pa
MMH injection	DPM injection	48 discrete-phase injection locations; local mass flow rate and initial velocity prescribed according to the circumferential injection arrangement; Rosin–Rammler droplet distribution of 8–60 μm with a mean diameter of 30 μm
NTO injection	DPM injection	48 discrete-phase injection locations; local mass flow rate and initial velocity prescribed according to the circumferential injection arrangement; Rosin–Rammler droplet distribution of 8–60 μm with a mean diameter of 30 μm
Continuous-phase inlet	None	No imposed continuous-phase mass inflow at the head end

Pressure monitoring point A was located near the wall, 2 mm downstream of the combustor head end. The pressure history recorded at this location was used for FFT and subsequent time–frequency analyses to characterize the principal pressure oscillations associated with rotating detonation.

Both liquid MMH and NTO were introduced into the computational domain through the DPM, without a continuous-phase mass-flow inlet. Droplet diameters followed a Rosin–Rammler (R–R) distribution ranging from 8 to 60 μm, with a mean diameter of 30 μm, representing the polydisperse droplet population produced by liquid–liquid impinging injection. The same droplet-size distribution parameters were employed for all comparative cases.

The pre-impingement MMH and NTO liquid jets and the primary liquid–liquid impingement-atomization process were not geometrically resolved in the present model. Therefore, the physical impingement angle between the two liquid jets was not used as an explicit numerical-model parameter. Instead, the post-primary-atomization spray was represented by a point-cone DPM injection released from each nominal impingement location. The spray-cone axis was aligned with the combustor axial direction, and a cone half-angle of 60° was prescribed. Four discrete particle streams were released from each point-cone injection. Under the baseline injection condition, the initial droplet velocity was 21.8 m/s. The droplet diameters followed the Rosin–Rammler distribution described above, with a range of 8–60 μm and a mean diameter of 30 μm. The baseline mass flow rates of MMH and NTO for each injector pair were approximately 5.95 and 10.71 g/s, respectively.

The spray was directed axially into the combustor rather than toward the combustor walls. Nevertheless, droplet–wall interaction was permitted when droplets reached a solid surface. All combustor walls employed the DPM wall-jet boundary condition; thus, droplets reaching a wall were treated using the wall-jet interaction model for their post-impact motion rather than being simply removed from the calculation. No resolved wall-film model was employed in the present simulations.

To investigate the effect of circumferentially non-uniform local injection conditions on the propagation direction of rotating detonation, the local injection parameters at different circumferential positions were varied while the combustor geometry, number of injection locations, total propellant mass flow rate, and overall oxidizer-to-fuel ratio were maintained constant. According to the injection intensity, the injector units were classified into low-intensity (S), baseline-intensity (M), and high-intensity (L) units. The M-type units employed the baseline injection parameters, whereas both the mass flow rate and initial injection velocity of the S- and L-type units were varied relative to those of the M-type units by prescribed proportions.

The non-uniformity amplitude, δ, is defined as follows:

$$\delta = \frac{m_M - m_S}{m_M} = \frac{m_L - m_M}{m_M} = \frac{v_M - v_S}{v_M} = \frac{v_L - v_M}{v_M}. \quad (16)$$

where m_S, m_M, and m_L denote the total propellant mass flow rates of a single S-, M-, and L-type injector pair, respectively, and v_S, v_M, and v_L denote their corresponding initial injection velocities. For the baseline uniform-injection condition, the total propellant mass flow rate was 800 g/s, and the overall oxidizer-to-fuel mass ratio (O/F) was fixed at 1.8. Because 48 injector pairs were uniformly distributed around the combustor circumference, the baseline total propellant mass flow rate of each M-type injector pair was 16.67 g/s, comprising approximately 5.95 g/s MMH and 10.71 g/s NTO. The initial injection velocity of both propellants was 21.8 m/s. These uniform-injection values were taken as the baseline parameters for the M-type injector units. The S- and L-type injector units were then defined by proportionally decreasing or increasing both the local mass flow rate and the initial injection velocity relative to the M-type values according to Equation (16). Because equal numbers of S-, M-, and L-type injector units are employed within each circumferential period and because the local injection parameters of MMH and NTO are varied by the same proportion, the total propellant mass flow rate and overall oxidizer-to-fuel ratio remain unchanged among the different non-uniform injection cases. Non-uniformity amplitudes of 0.2, 0.4, and 0.6 are investigated in the present study.

In the present parameterization, δ represents a coupled circumferential variation of the local propellant mass flow rate and initial injection velocity. This prescription was adopted with practical injector implementation in mind: adjusting local injector-orifice characteristics can modify both the local flow capacity and injection condition while retaining the same overall impinging-injector arrangement.

To provide a theoretical reference for the detonation propagation velocity, an equilibrium Chapman–Jouguet (CJ) calculation was performed for the overall MMH/NTO mixture used in the present simulations. The oxidizer-to-fuel mass ratio was set to $O/F = 1.8$, consistent with all comparative cases. The initial reactant temperature was set to 298.15 K, and a representative initial pressure of 0.3 MPa was adopted based on the time-averaged pressure level in the near-head-end propellant-replenishment region. Liquid MMH and N_2O_4 were defined using their liquid-phase thermodynamic properties, and the equilibrium CJ state was solved using the NASA CEA detonation solver. Under these conditions, the theoretical CJ detonation velocity was calculated to be 2495.96 m/s.

2.3. Numerical Resolution Sensitivity Analysis

A numerical resolution sensitivity analysis was conducted before the parametric simulations to evaluate the effects of spatial and temporal discretization on the calculated results. Because the time step in rotating-detonation simulations must be appropriately matched to the local grid size, different time steps were employed for different grids to maintain comparable CFL numbers among the simulations. The sensitivity of the principal detonation-propagation characteristics to numerical resolution was evaluated by comparing the peak pressure, dominant pressure frequency, and pressure histories obtained using different combinations of spatial and temporal resolutions.

Because both grid spacing and time step vary in this three-grid comparison, it is interpreted here as a combined spatial–temporal resolution assessment. A separate fixed-grid time-step sensitivity assessment of the transient establishment process is presented later, together with the corresponding wave-competition analysis.

Three structured grids, referred to as the coarse, medium, and fine grids, were generated using approximately 0.70, 1.80, and 2.50 million cells, respectively. As the grid spacing

was reduced, the corresponding time step was also decreased. The grid sizes and associated time steps are summarized in Table 3. The same computational model, physical models, and boundary conditions were applied to all three resolution levels.

Table 3. Numerical resolution combinations and corresponding computational results.

Grid	Number of Cells (10^4)	Time Step (s)	Peak Pressure (MPa)	Dominant Pressure Frequency (Hz)	Relative Error (%)
Coarse	70	7×10^{-7}	1.4–1.6	7115	−2.8
Medium	180	6×10^{-7}	1.4–1.6	7266	−0.8
Fine	250	4×10^{-7}	1.5–1.6	7323	—

As shown in Table 3, the dominant pressure frequency gradually converges with increasing numerical resolution. The dominant frequencies obtained using the coarse, medium, and fine resolutions are 7115, 7266, and 7323 Hz, respectively. Taking the fine-resolution result as the reference, the relative deviation of the dominant frequency obtained with the medium resolution is less than 1%, while the corresponding peak-pressure range is also close to that obtained with the fine resolution. These results indicate that further refinement of the spatial and temporal resolutions produces only minor changes in the principal pressure-oscillation characteristics.

Figure 4 compares the pressure histories at monitoring point A for the three numerical resolutions. Stable periodic pressure oscillations are obtained for all three resolution combinations, with generally similar peak pressures and oscillation periods. Increasing the resolution from the medium to the fine level results in only minor changes in the pressure waveform and its principal oscillation characteristics, indicating that the medium resolution is sufficient to capture the major rotating-detonation pressure response of interest in the present study.

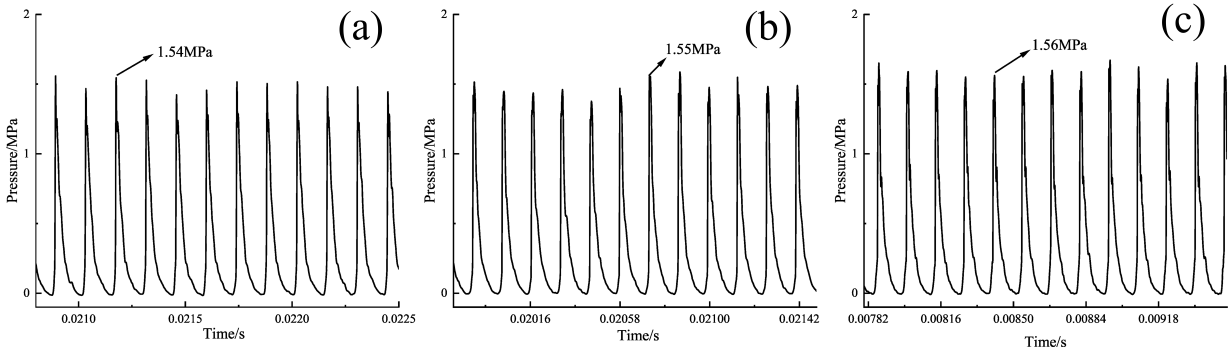


Figure 4. Pressure histories at monitoring point A obtained using different numerical resolutions: (**a**) coarse resolution; (**b**) medium resolution; (**c**) fine resolution.

Considering the dominant pressure frequency, peak pressure, and pressure-history characteristics, together with the balance between computational accuracy and computational cost, the medium resolution with approximately 1.8 million cells and its corresponding time step was adopted for subsequent simulations.

3. Results and Discussion

To investigate the effect of circumferentially non-uniform injection on rotating-detonation propagation-direction selection, repeated simulations were performed for different injection configurations. The resulting propagation directions are summarized in Table 4.

For each injection configuration, the repeated simulations employed the same combustor geometry, computational grid, numerical schemes, macroscopic boundary conditions, total propellant mass flow rate, overall oxidizer-to-fuel ratio, and prescribed circumferential injection arrangement. No artificial CW- or CCW-oriented pressure/temperature disturbance or prescribed directional initiation was imposed. MMH and NTO droplets were introduced through the DPM, and the subsequent hypergolic reaction, pressure-wave formation, and rotating-detonation establishment were allowed to develop naturally.

Although the prescribed macroscopic conditions and Rosin–Rammler distribution parameters were identical among repeated runs, the discrete droplet parcels were stochastically sampled from the prescribed size distributions. Consequently, independently started simulations contained different instantaneous microscopic droplet-field realizations. These small discrete-phase perturbations subsequently interacted nonlinearly with droplet evaporation, hypergolic reaction, and the developing pressure-wave field during the highly transient establishment stage. Thus, repeated simulations were used to assess the robustness of the directional preference under these naturally occurring microscopic perturbations. No directional bias was deliberately introduced between repeated simulations. For reproducibility, each repeated simulation was independently restarted under identical macroscopic conditions, and the DPM parcels were regenerated according to the prescribed Rosin–Rammler droplet-size distribution, resulting in different instantaneous droplet-field realizations.

Table 4. Propagation-direction selection under different circumferential injection configurations and non-uniformity amplitudes.

Case	Injection Arrangement	δ	Repeated Simulation Results	Direction-Selection Behavior
Case 1	S_1–M_1–L_1	0.2	Three simulations with the CW arrangement did not yield a consistent propagation direction; the same was observed for the CCW arrangement.	No consistent directional preference
Case 2	S_2–M_2–L_2	0.2	Three simulations with the CW arrangement did not yield a consistent propagation direction; the same was observed for the CCW arrangement.	No consistent directional preference
Case 3	S_1–M_1–L_1	0.4	Three simulations with the CW arrangement did not yield a consistent propagation direction; the same was observed for the CCW arrangement.	No consistent directional preference
Case 4	S_2–M_2–L_2	0.4	Five simulations with the CW arrangement did not yield a consistent propagation direction; the same was observed for the CCW arrangement.	No consistent directional preference
Case 5	S_4–M_4–L_4	0.4	All five simulations for both CW and CCW arrangements produced propagation in the corresponding arrangement direction.	Consistent directional preference
Case 6	S_4–M_4–L_4	0.6	All three simulations for both CW and CCW arrangements produced propagation opposite to the corresponding arrangement direction.	Opposite-direction propagation in the tested runs

Although the selected CW/CCW propagation direction differed among some repeated simulations, all repeated simulations in Cases 1–6 ultimately developed into a stable single-wave rotating-detonation mode.

3.1. Effect of Circumferentially Non-Uniform Injection on the Rotating-Detonation Propagation Direction

Case 5 with the S_4–M_4–L_4 configuration was first selected for detailed analysis. In this configuration, four consecutive injector units are assigned to each of the S-, M-, and L-type injection intensities, forming one S_4–M_4–L_4 injector group. Four such groups, comprising a total of 48 injector units, are periodically distributed around the circumference. This arrangement provides a relatively long continuous circumferential extent for each injection-intensity level. Figure 5 illustrates the injector-unit distribution for the CW arrangement.

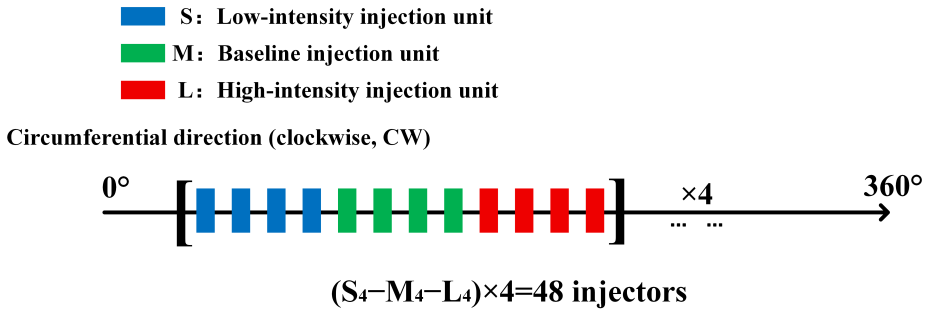


Figure 5. Schematic of the S_4–M_4–L_4 circumferentially non-uniform injection configuration for Case 5 (clockwise (CW) arrangement). The ellipsis denotes repetition of the periodic injector-unit pattern and does not affect scientific understanding.

To illustrate the local mixture-formation process under the circumferentially non-uniform injection condition, a non-reacting simulation of Case 5 was examined on a visualization plane passing through the central two adjacent injector units within one S-type region of the S_4–M_4–L_4 arrangement. Figure 6 presents the evolution of the MMH and NTO droplet parcels and their corresponding vapor mass-fraction distributions at t = 150, 300, 450, and 600 μs. The dispersed and vapor phases develop progressively with time, while the broader vapor distributions also reflect transport and mixing associated with the neighboring L- and M-type injection regions.

The viewing direction is defined along the combustor axis from the head end toward the outlet. Accordingly, a detonation wave propagating clockwise in the projection onto the head-end plane is defined as clockwise (CW) propagation, whereas propagation in the opposite direction is defined as counterclockwise (CCW). In the circumferentially unwrapped plots, the arc-length coordinate increases from the initial reference position in the CW direction. Therefore, propagation toward increasing arc length corresponds to CW propagation, whereas propagation toward decreasing arc length corresponds to CCW propagation.

Figure 7 shows the evolution of the outer-wall pressure as the detonation wave passes through one injector group during stable propagation under the CW circumferential injection arrangement. Despite the periodic local variations in injection conditions around the circumference, the detonation-wave front remains continuous and intact, without pronounced wave-front splitting or propagation instability. As the detonation wave propagates circumferentially, the local intensity and spatial extent of the high-pressure region vary periodically. This behavior indicates that circumferentially non-uniform injection modulates the local pressure structure of the stable rotating detonation without disrupting the self-sustained propagation of the single-wave mode under the present operating condition.

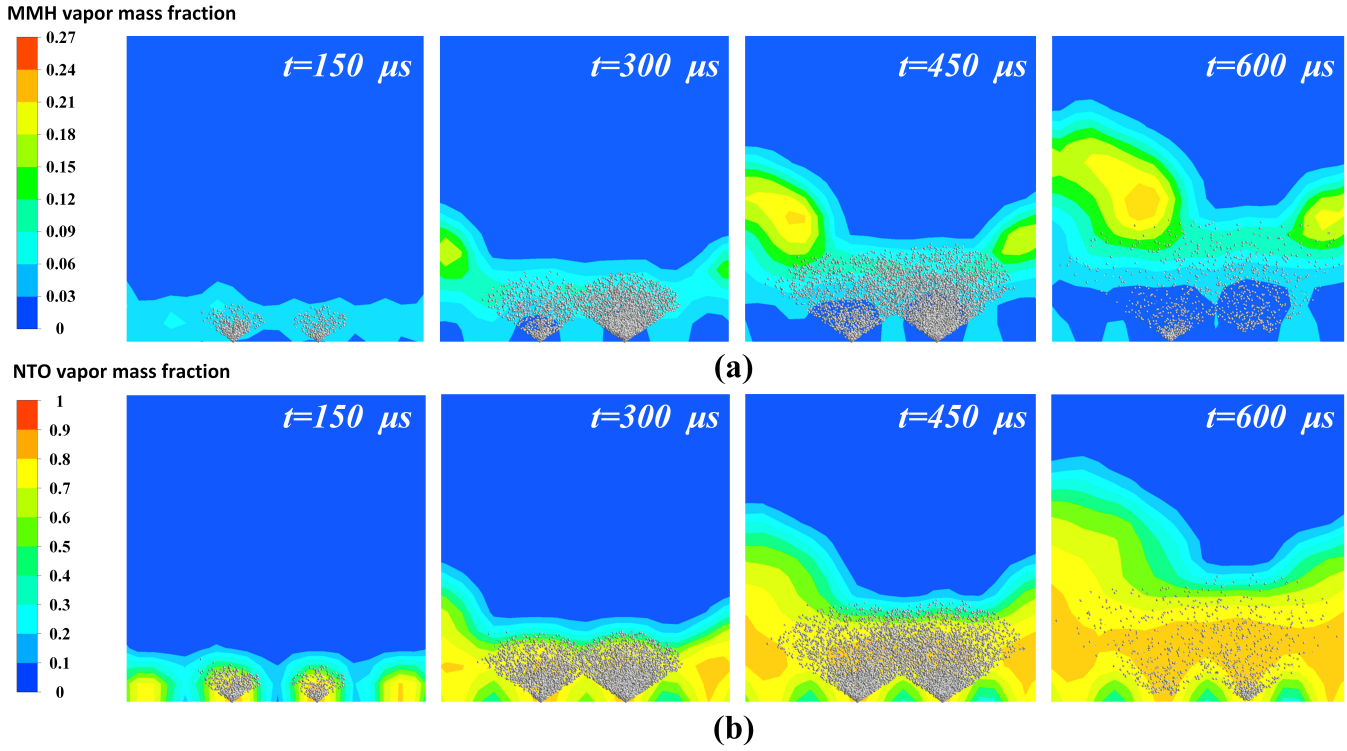


Figure 6. Temporal evolution of the dispersed and vapor phases under non-reacting conditions in the vicinity of two adjacent S-type injector units in Case 5: (**a**) MMH; (**b**) NTO. Droplet parcels within a thin layer adjacent to the visualization plane are superimposed on the corresponding vapor mass-fraction contours.

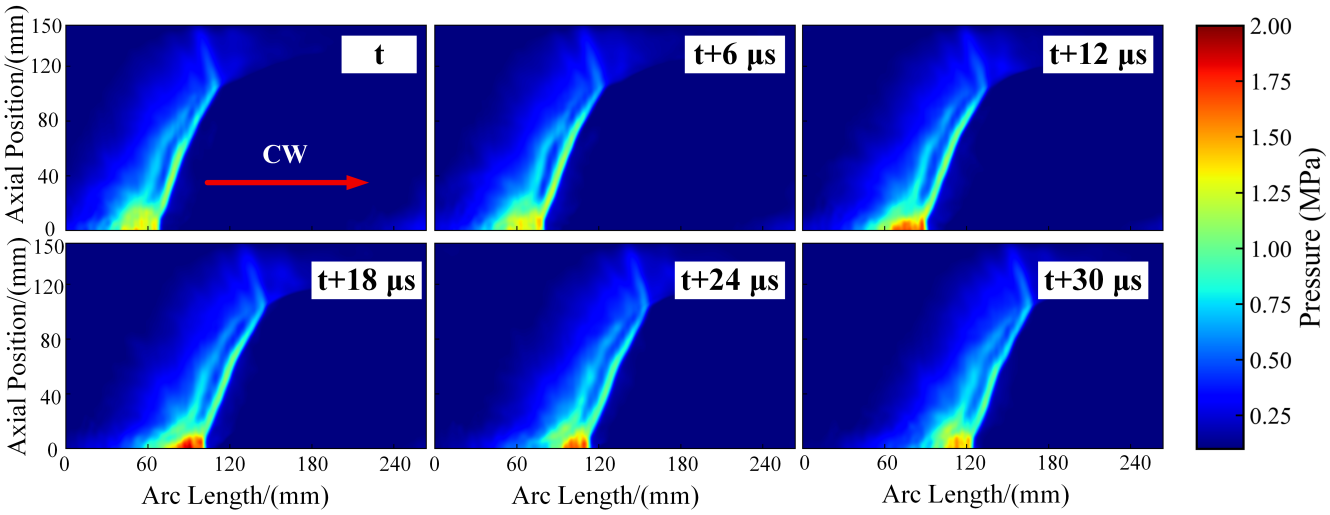


Figure 7. Temporal evolution of the outer-wall pressure over one injector group for Case 5 under the CW circumferentially non-uniform injection arrangement. The arrow indicates the CW propagation direction.

To further examine the relationship between the local pressure response and injection distribution during stable propagation, Figure 8 presents the circumferentially unwrapped pressure distribution near the DPM injection locations, with the positions of the different injection-intensity regions indicated. Each S, M, and L region marked in the figure contains four corresponding injector units. As the detonation wave successively passes through the S-, M-, and L-type injection regions, the local extent and intensity of the high-pressure region exhibit corresponding periodic variations. This result demonstrates that, even

after stable unidirectional rotating detonation has been established, differences in local propellant supply continue to modulate the pressure structure of the detonation wave. Their specific influence is further examined through the injection-arrangement reversal discussed below.

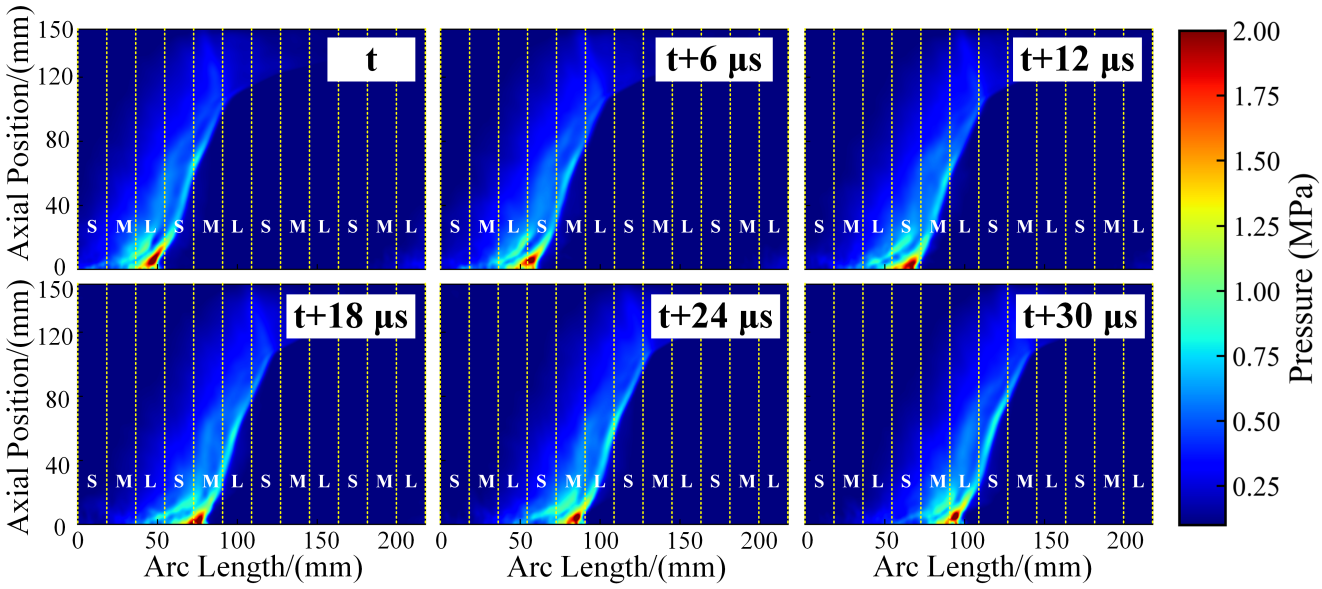


Figure 8. Temporal evolution of the circumferentially unwrapped pressure distribution near the DPM injection locations over one injector group for Case 5 under the CW circumferentially non-uniform injection arrangement.

To further investigate the relationship between the injection arrangement direction and the resulting detonation propagation direction, the arrangement direction of the S_4–M_4–L_4 configuration was reversed, while the non-uniformity amplitude, injection parameters, and circumferential injector-group length were maintained unchanged. As shown in Figure 9, reversing the injection arrangement resulted in a corresponding change in the final propagation direction from CW to CCW. Repeated simulations further showed that all five simulations with the CW arrangement developed CW rotating detonation, whereas all five simulations with the reversed arrangement developed CCW rotating detonation. Within the range of repeated simulations considered in this study, this configuration therefore exhibits a high degree of consistency in propagation-direction selection.

These results demonstrate a clear correspondence between the final rotating-detonation propagation direction and the arrangement direction of the circumferential injection-intensity distribution for the specified non-uniformity amplitude and injector-group length. Thus, modifying the circumferential distribution of local injection conditions can influence the selection of the dominant propagation direction during rotating-detonation establishment.

To further assess whether the outlet boundary treatment influences propagation-direction selection, an additional outlet-boundary sensitivity calculation was performed for Case 5 (S_4–M_4–L_4, $\delta = 0.4$) with the CW injection arrangement. As shown in Figure 10, a large buffer volume was attached downstream of the physical combustor exit, and the pressure-outlet boundary was relocated to the outer boundary of the buffer volume, while the other computational conditions were kept unchanged. Although some differences in the instantaneous pressure magnitude and local pressure-wave structure are observed between the two configurations, both cases develop into a stable single-wave rotating-detonation mode with the same CW propagation direction. The dominant pressure frequencies are also both approximately 7.2 kHz. These results indicate that the propagation-direction selection observed for Case 5 is retained under the extended-buffer outlet treatment.

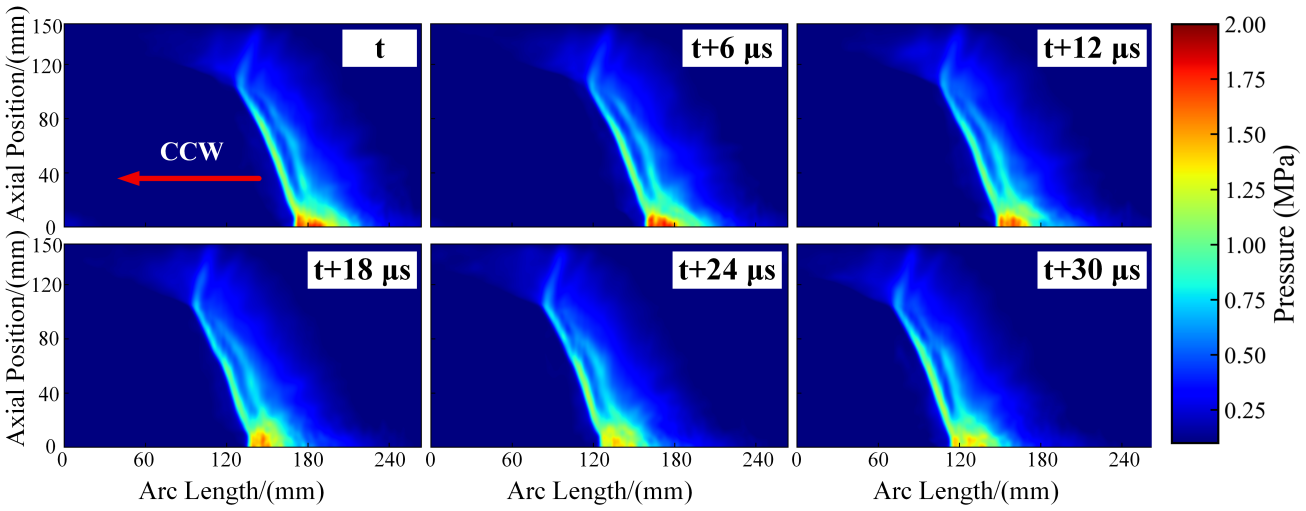


Figure 9. Temporal evolution of the outer-wall pressure over one injector group for Case 5 under the CCW circumferentially non-uniform injection arrangement. The arrow indicates the CCW propagation direction.

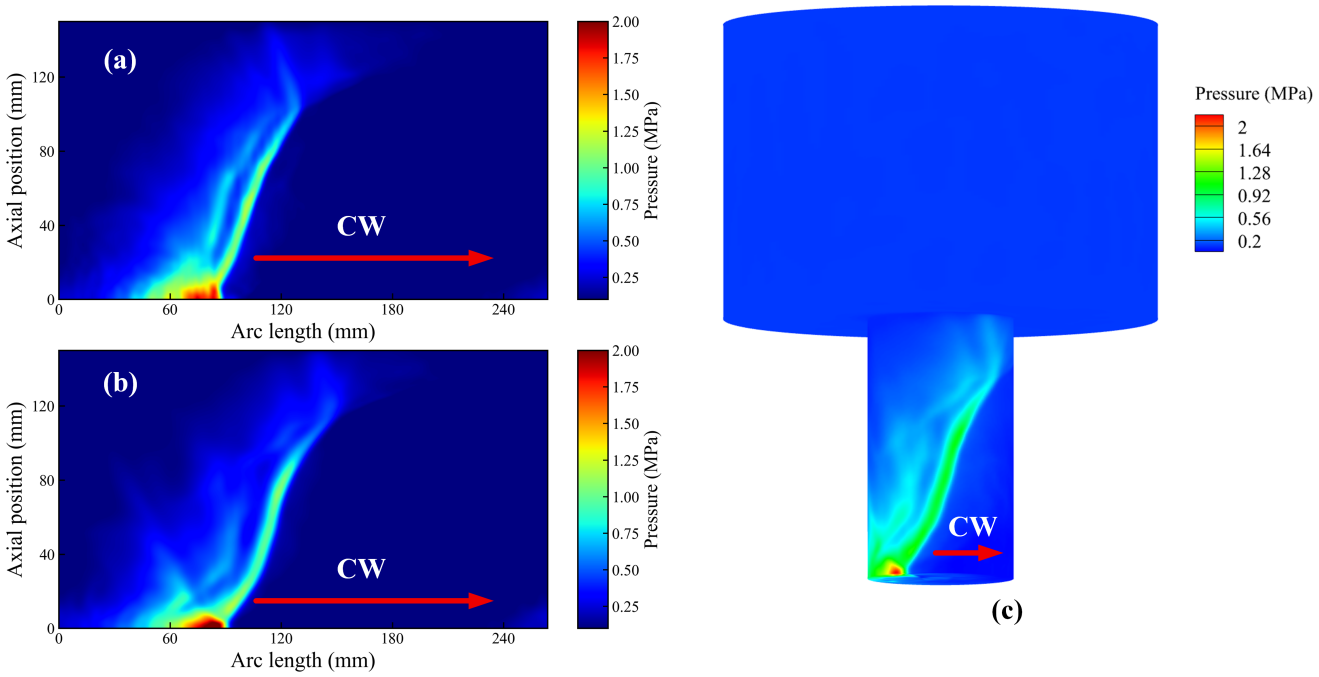


Figure 10. Outlet-boundary sensitivity assessment for Case 5: representative quasi-steady pressure fields obtained with (**a**) the original outlet configuration and (**b**) the extended-buffer configuration; (**c**) three-dimensional view of the complete computational domain with the downstream buffer volume. The arrows indicate the CW propagation direction.

To examine whether a circumferential variation in injection velocity is necessary for the arrangement-following result, one additional simulation was performed for the CW arrangement of Case 5. The prescribed circumferential mass-flow-rate distribution was retained, while the initial injection velocity was kept identical among the S-, M-, and L-type injector units. The resulting rotating detonation propagated in the CW direction, consistent with the prescribed CW injection arrangement. Thus, arrangement-following propagation was also obtained in this fixed-velocity realization. Because only one such realization was examined, this result is used here as supplementary evidence. The relative effects

associated with local propellant replenishment and injection momentum will be examined systematically in future work.

3.2. Effects of Circumferential Injector-Group Length and Non-Uniformity Amplitude on Propagation-Direction Selection

To further identify the conditions under which circumferential injection non-uniformity influences propagation-direction selection, the results obtained with different non-uniformity amplitudes and circumferential injector-group lengths were compared. The combustor geometry, injection locations, total number of injector units, and total propellant mass flow rate were kept unchanged. Three representative arrangements—S_1–M_1–L_1, S_2–M_2–L_2, and S_4–M_4–L_4—were constructed by varying the number of consecutive circumferential positions occupied by each S-, M-, and L-type injector unit. These configurations were used to examine how the circumferential extent of the local injection differences affects the final propagation-direction selection. The results are summarized in Table 4.

In the S_1–M_1–L_1 arrangement, the S-, M-, and L-type injector units are distributed sequentially, with each injection intensity occupying only one consecutive injection position. Each injector group therefore consists of three injection positions, resulting in 16 groups around the circumference. In the S_2–M_2–L_2 arrangement, each injection intensity occupies two consecutive positions, giving six injection positions per group and eight groups around the circumference. In the S_4–M_4–L_4 arrangement, each injection intensity occupies four consecutive positions, resulting in 12 injection positions per group and four groups around the circumference. Thus, from S_1–M_1–L_1 to S_4–M_4–L_4, the circumferential length of an individual injector group increases progressively, while the total number of injector groups around the circumference decreases.

As shown in Table 4, at a non-uniformity amplitude of 0.2, both the S_1–M_1–L_1 and S_2–M_2–L_2 configurations, which have relatively short circumferential injector-group lengths, produce different propagation directions among the repeated simulations and therefore show no consistent directional preference. When the non-uniformity amplitude is increased to 0.4, the repeated simulations of the S_1–M_1–L_1 and S_2–M_2–L_2 configurations still do not consistently produce propagation in the corresponding injection arrangement direction. These results indicate that, under the conditions considered here, simply increasing the difference in local injection parameters is insufficient to ensure consistent selection of the final propagation direction. The circumferential spatial extent over which the local injection difference persists also plays an important role.

In contrast, at a non-uniformity amplitude of 0.4, the S_4–M_4–L_4 configuration provides a longer continuous circumferential extent for each injection-intensity level, allowing the local propellant-supply difference to persist over a greater circumferential distance. In all repeated simulations considered here, the final propagation direction was consistent with the injection arrangement direction. The S_4–M_4–L_4 configuration therefore exhibits substantially greater consistency in direction selection than the S_1–M_1–L_1 and S_2–M_2–L_2 configurations.

Physically, a longer continuous injection-intensity region allows local differences in propellant replenishment, droplet vaporization, and heat release to persist over a greater circumferential distance, whereas the local differences associated with shorter S/M/L regions are more readily smoothed by circumferential transport and mixing. Because the competing CW and CCW waves traverse the S/M/L regions in opposite sequences, increasing the continuous circumferential extent of these regions provides a more persistent asymmetric environment for their development. The resulting difference in the replenishment and heat-release histories experienced by the two wave systems can accumulate over a longer interaction distance, thereby improving the consistency of propagation-direction selection.

To provide a preliminary assessment of the propagation response at a larger non-uniformity amplitude, the amplitude of the S_4–M_4–L_4 configuration was further increased to 0.6 in Case 6.

According to Equation (16), the prescribed mass flow rates and initial injection velocities of the S/M/L units are, respectively, 0.6, 1.0, and 1.4 times the M-type baseline values in Case 5 ($\delta = 0.4$) and 0.4, 1.0, and 1.6 times the baseline values in Case 6 ($\delta = 0.6$). Thus, Case 6 imposes a substantially stronger local injection contrast. For example, for an S-type injector pair, the total propellant mass flow rate decreases from approximately 10.00 g/s in Case 5 to 6.67 g/s in Case 6, while the initial injection velocity decreases from 13.08 to 8.72 m/s. Case 6 is therefore examined here as an exploratory high-non-uniformity condition.

Figure 11 shows the outer-wall pressure evolution for a representative simulation with the CW arrangement. The high-pressure front propagates circumferentially toward decreasing arc length, corresponding to CCW rotating detonation. Thus, in this case, the final detonation propagation direction is opposite to the injection arrangement direction. Compared with the relatively continuous and regular single-wave structure observed in Case 5, the detonation-wave front in Case 6 exhibits more pronounced curvature and local distortion, while the shape and spatial extent of the high-pressure region vary more strongly during propagation. Under the present Case 6 condition, the larger local injection difference is accompanied by stronger modulation of the local structure of the established detonation wave.

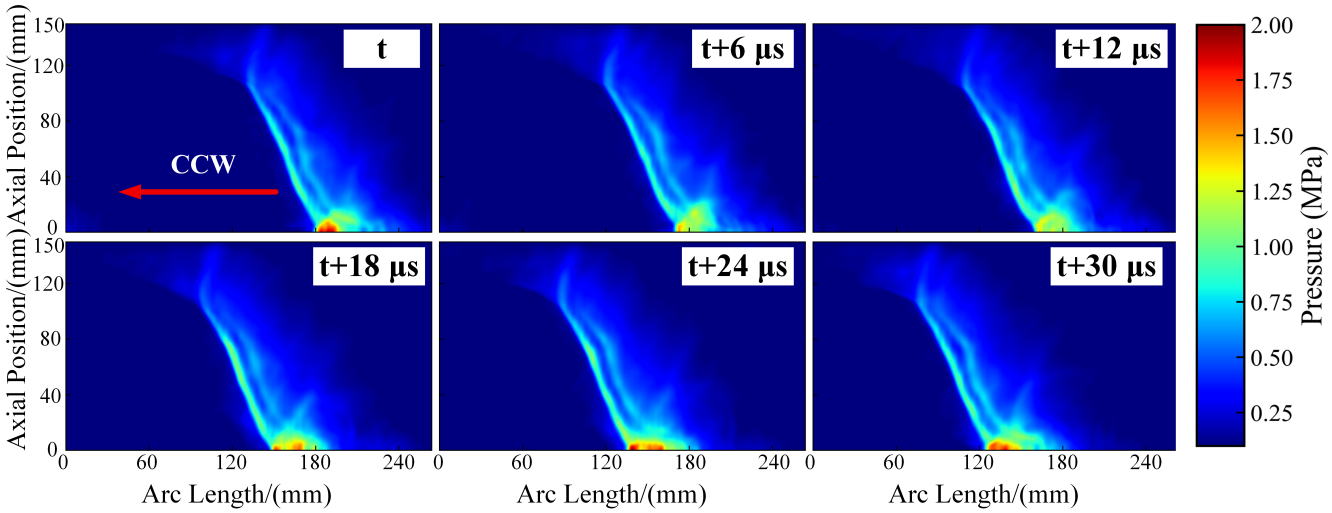


Figure 11. Temporal evolution of the outer-wall pressure over one injector group for CCW rotating detonation in Case 6 under the CW circumferentially non-uniform injection arrangement. The arrow indicates the CCW propagation direction.

At $\delta = 0.6$, three repeated simulations were performed for each of the CW and CCW injection arrangements, and propagation opposite to the corresponding injection arrangement direction was observed in all tested runs. Compared with the consistent arrangement-following propagation obtained at $\delta = 0.4$, this result indicates a non-monotonic directional response to the non-uniformity amplitude under the investigated conditions. The opposite-direction behavior is therefore reported here as an observed response of Case 6, without extending it to a general trend with increasing δ. All repeated simulations, including Case 6, eventually developed into a stable single-wave rotating detonation mode during the quasi-steady stage. Although different CW/CCW propagation directions were obtained among repeated simulations, no persistent multi-wave mode or wave-splitting behavior was observed.

Overall, the influence of circumferentially non-uniform injection on rotating-detonation propagation-direction selection depends on both the non-uniformity amplitude and the circumferential injector-group length. At a non-uniformity amplitude of 0.4, increasing the continuous circumferential extent of a given injection-intensity level substantially improves the consistency of direction selection. The opposite-direction propagation observed for Case 6 therefore represents a non-monotonic directional response under the investigated conditions. The coupled effects of these parameters require further investigation.

3.3. Rotating-Detonation Response to Reversal of the Injection Arrangement

The preceding results demonstrate that circumferentially non-uniform injection can influence propagation-direction selection during rotating-detonation establishment. It remains unclear whether reversing the injection arrangement after stable unidirectional rotating detonation has been established can alter the propagation direction. To investigate this issue, the original S_4–M_4–L_4 injection arrangement was reversed to L_4–M_4–S_4 after stable rotating detonation had been established, while all other injection parameters and boundary conditions were maintained unchanged. The response of the rotating detonation to this reversal was then examined.

The results show that the established rotating detonation does not switch its propagation direction after reversal of the injection arrangement but instead continues to propagate in its original direction. This result indicates that, compared with the establishment stage, a stable unidirectional rotating detonation exhibits a more pronounced tendency to retain its established propagation direction.

To further characterize the dynamic response of the established rotating detonation to the change in injection arrangement, a sliding fast Fourier transform (SFFT) was applied to the wall-pressure signal for time–frequency analysis. A sliding window containing 5120 sampling points, corresponding to a duration of 3.072 ms, was employed. Adjacent windows were shifted by 256 sampling points, corresponding to a time interval of 0.1536 ms. A Hann window was applied to the pressure signal within each analysis window, and the dominant frequency was identified within the range of 6.5–7.6 kHz. This frequency range was selected to encompass the dominant pressure-frequency band of the stable rotating detonation, which is approximately 7.2 kHz under the present operating conditions, and to track its evolution during the injection-arrangement reversal. To reduce the influence of finite frequency resolution on spectral-peak identification, quadratic interpolation was applied to the maximum-amplitude frequency bin and its adjacent bins to refine the estimated peak location. The resulting time history of the dominant frequency was subsequently smoothed using a Savitzky–Golay filter with a 7-point window and a third-order polynomial.

The resulting evolution of the dominant frequency is shown in Figure 12. Before reversal of the injection arrangement, the estimated dominant pressure frequency remains stable at approximately 7.18 kHz. After the reversal, the dominant-frequency trajectory does not exhibit an instantaneous discontinuity; instead, it gradually shifts toward a lower frequency over a finite period and eventually stabilizes at approximately 7.06 kHz. It should be noted that these dominant frequencies were obtained from the spectral peaks of the sliding-window analysis after quadratic-interpolation correction and are primarily used to characterize the dynamic response of the pressure-oscillation behavior to the change in injection arrangement. The SFFT results therefore indicate that, although reversal of the injection arrangement is insufficient to immediately alter the established propagation direction, it nevertheless causes a measurable adjustment of the pressure-oscillation characteristics.

It is worth noting that, under uniform injection, the dominant pressure frequency of the stable rotating detonation is approximately 7.2 kHz, whereas that under the original

S_4–M_4–L_4 non-uniform injection condition is approximately 7.18 kHz. The difference between these values is relatively small, indicating that the introduction of the present circumferentially non-uniform injection distribution does not produce a pronounced shift in the dominant frequency during stable propagation under the operating conditions considered. By contrast, after reversal of the injection arrangement, the dominant frequency gradually decreases to approximately 7.06 kHz. This result indicates that, even though the propagation direction is retained, the propagation state of the detonation wave still undergoes adjustment in response to changes in the local propellant-supply relationship.

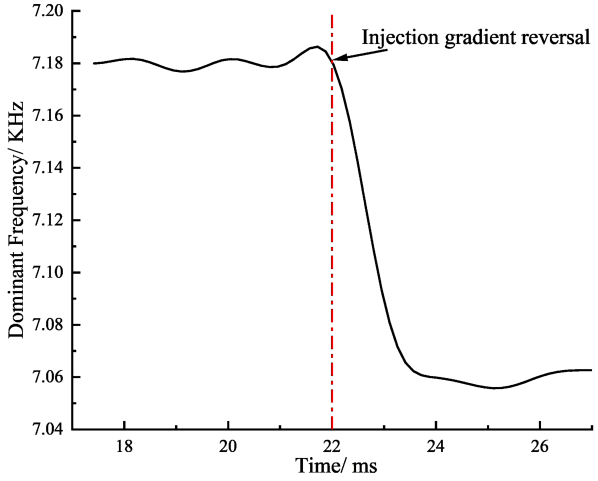


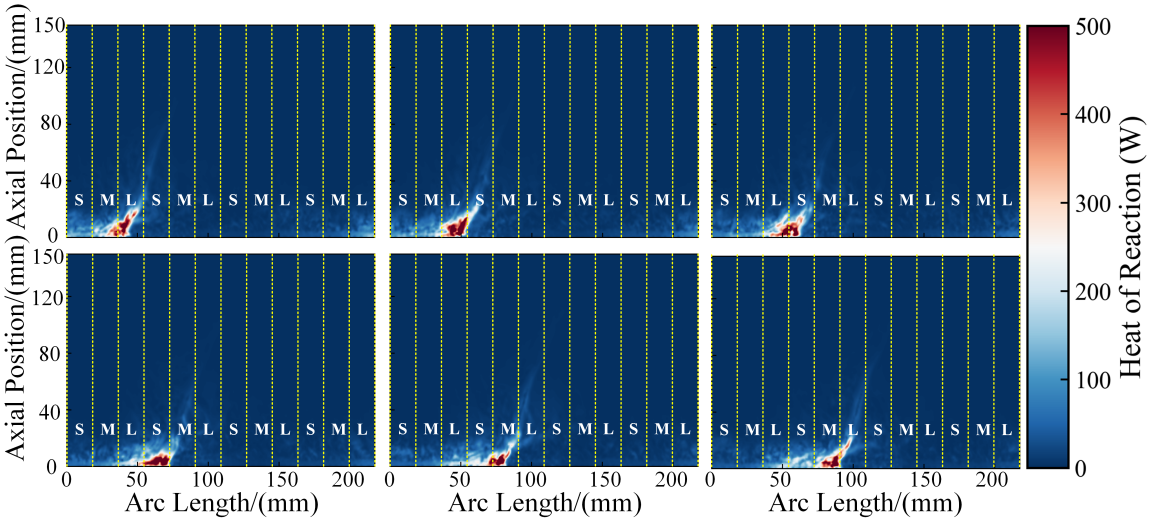
Figure 12. Evolution of the dominant pressure frequency during reversal of the injection arrangement.

To further examine the flow-field response associated with the change in dominant frequency, Figure 13 compares the heat-release distributions over one injection-arrangement period before and after reversal. Pronounced high-heat-release regions are maintained under both arrangements, and no fundamental change in the overall rotating-detonation structure is observed. However, differences are evident in the local position and spatial distribution of the high-heat-release regions. These differences indicate that reversal of the injection arrangement modifies the local reaction process experienced by the detonation wave as it successively passes through regions with different injection intensities.

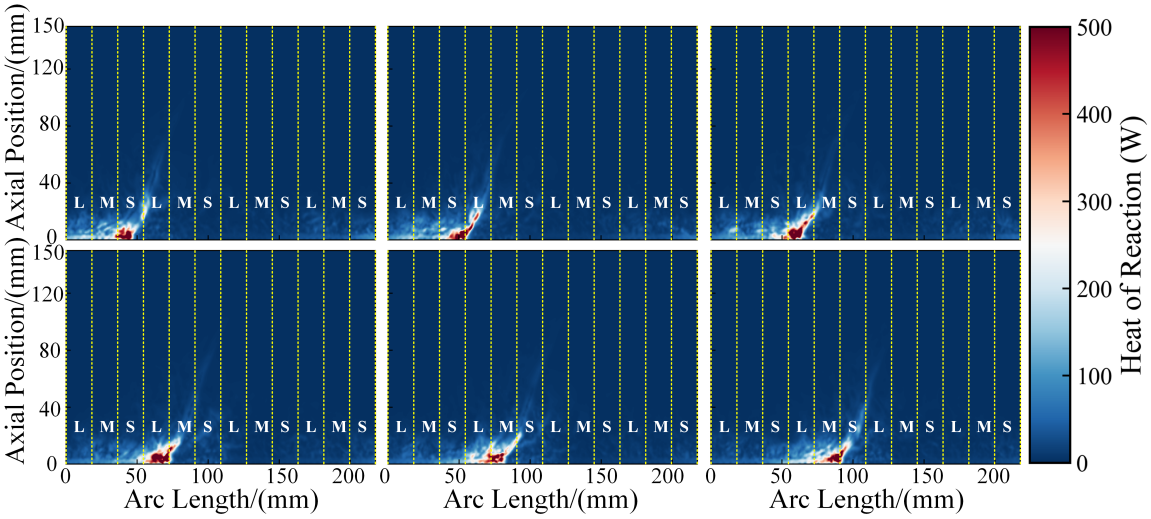
The time-averaged temperature distribution in the DPM injection region was further compared, as shown in Figure 14. Because low-temperature droplets are continuously supplied to the combustor, distinct low-temperature regions form near the injection locations. After reversal of the injection arrangement, the circumferential distribution of these low-temperature regions changes according to the positions of the different local injection intensities, indicating that the droplet replenishment, heating, and evaporation environments encountered by the propagating detonation wave are modified. The redistribution of the local thermal state and propellant-supply conditions corresponds to the changes in heat-release location shown in Figure 13. This correspondence indicates that reversal of the injection arrangement continuously modulates the local propellant replenishment and reaction processes within the established rotating detonation.

Overall, reversing the injection arrangement does not cause the established rotating detonation to switch its propagation direction. It does, however, change the dominant pressure frequency, local heat-release distribution, and thermal state of the injection region. These results indicate that circumferentially non-uniform injection plays different roles during different stages of rotating-detonation development. During the establishment stage, it can influence the selection of the dominant propagation direction. After stable unidirectional rotating detonation has been established, its influence is manifested primarily

through modulation of local propellant replenishment, reaction processes, and pressure response. This behavior further suggests that selection of the propagation direction occurs predominantly before the rotating detonation is fully established.



(**a**)



(**b**)

Figure 13. Comparison of the heat-release distributions before and after reversal of the injection arrangement: (**a**) S_4–M_4–L_4 arrangement; (**b**) L_4–M_4–S_4 arrangement.

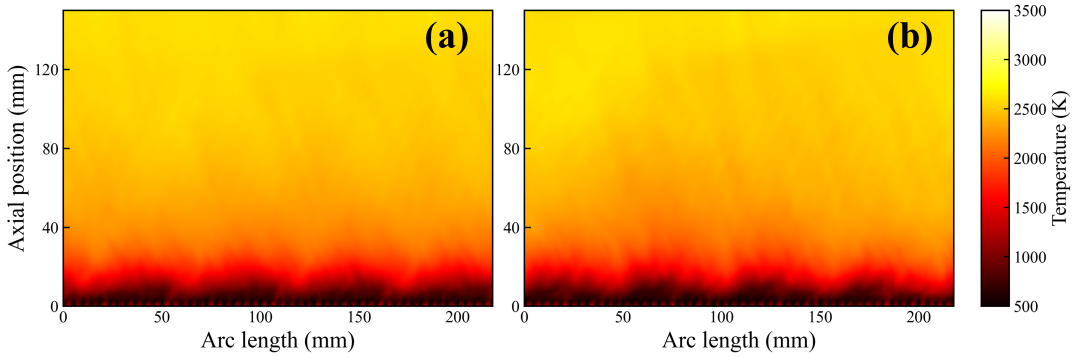


Figure 14. Time-averaged temperature distributions in the DPM injection region before and after reversal of the injection arrangement: (**a**) S_4–M_4–L_4 arrangement; (**b**) L_4–M_4–S_4 arrangement.

3.4. Wave-System Evolution and Propagation-Direction Selection During Rotating-Detonation Establishment

To further investigate how circumferentially non-uniform injection influences propagation-direction selection, the CW-arrangement condition of Case 5 was selected for high-temporal-resolution analysis. This case develops into stable CW rotating detonation, and its transient pressure field was examined during the establishment stage. Figure 15 shows the evolution of the pressure field on the transverse cross-section at the combustor head end, perpendicular to the combustor axis, during a representative detonation-establishment process. For convenience, the instant at which a distinct local high-pressure core first forms is denoted as t. It should be emphasized that a stable rotating detonation wave has not yet formed during the early stage. The following analysis therefore focuses primarily on the formation, propagation, and competition of circumferential pressure structures and their relationship with the eventual propagation direction.

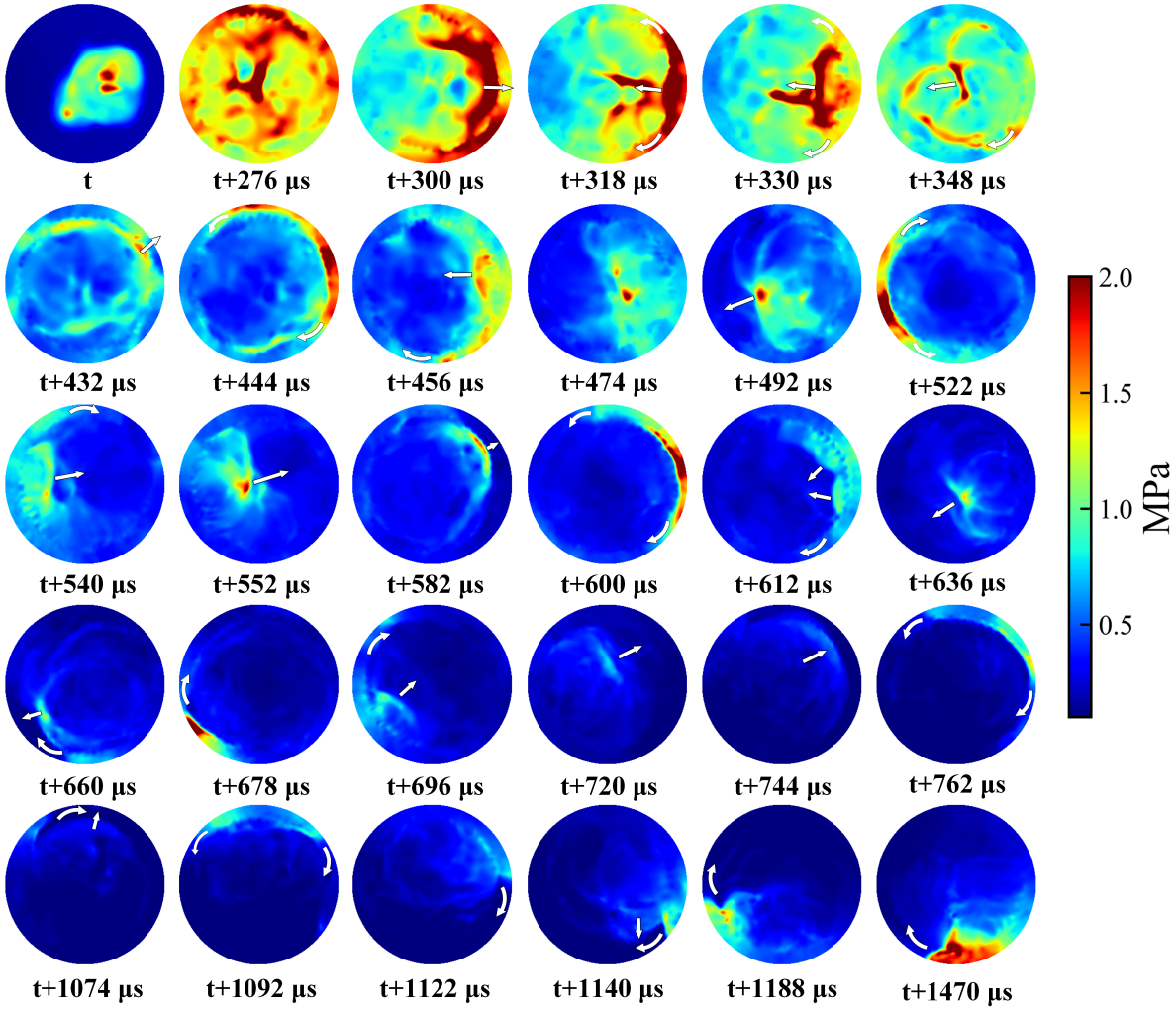


Figure 15. Transient evolution of the pressure field on the transverse cross-section at the combustor head end during rotating-detonation establishment under circumferentially non-uniform injection. Curved arrows indicate circumferentially propagating pressure waves, and straight arrows indicate radially propagating pressure waves.

A local high-pressure core first forms during the initial stage, after which the pressure disturbance rapidly expands into the surrounding region. By t + 276 μs, a large-scale non-uniform pressure distribution has developed within the combustor; however, the wave system remains highly irregular, and no stable circumferentially propagating structure has

yet emerged. As the disturbance continues to evolve, between t + 300 and 348 μs, portions of the pressure waves propagate outward while simultaneously developing in two opposite circumferential directions. During this stage, weak but identifiable circumferential pressure waves are present in both the CW and CCW directions, accompanied by radially outward-propagating pressure waves. This behavior indicates that the final rotating-detonation propagation direction is not determined immediately upon formation of the local high-pressure core but instead emerges progressively during the subsequent evolution of the circumferential wave system.

During t + 432–762 μs, the pressure structures within the combustor undergo repeated amplification and attenuation, while the oppositely propagating circumferential pressure waves continuously interact with radial pressure waves. The two circumferential components do not evolve symmetrically. The CCW-propagating wave system gradually weakens, whereas the circumferential pressure structure propagating in the CW direction persists and subsequently becomes re-amplified. These observations indicate that a distinct competition between oppositely propagating circumferential wave systems occurs before stable rotating detonation is established and that the dominant propagation direction develops progressively during this stage.

Following this early competition, the CW-propagating pressure wave gradually becomes dominant. During t + 1074–1188 μs, the overall pressure level within the combustor remains relatively low; nevertheless, the circumferential pressure structure propagating in the CW direction continues to persist and interacts with other radial or transverse pressure structures in the combustor. The circumferential pressure wave subsequently strengthens further, and a pronounced high-pressure front emerges at approximately t + 1470 μs, eventually developing into the stable single-wave rotating detonation described above. The establishment process can therefore be summarized as follows: formation of a local pressure disturbance → generation of oppositely propagating circumferential pressure waves → competition between the two wave systems → retention of the dominant propagation direction → further amplification of the circumferential pressure structure → establishment of stable rotating detonation.

The above evolution demonstrates that the final propagation direction develops progressively through competition between circumferential pressure waves propagating in opposite directions. In Case 5, the CW- and CCW-propagating pressure waves pass through the S-, M-, and L-type injection regions in opposite sequences and therefore experience different sequences of local propellant replenishment, droplet evaporation, and reaction environments. These circumferential differences in propellant-supply conditions provide different development environments for the two oppositely propagating pressure-wave systems. In the present case, the CCW pressure structure gradually decays, whereas the CW structure is retained and subsequently strengthened, ultimately developing into stable single-wave rotating detonation.

It should be emphasized that the transient pressure fields presented here directly reveal the generation, competition, and relative strengthening or weakening of the oppositely propagating pressure waves. However, these pressure-field results alone are insufficient to isolate the individual contributions of local injection, droplet evaporation, and heat release to the development of the two wave systems. Accordingly, the present results are more appropriately interpreted as evidence that circumferentially non-uniform injection participates in the early wave-competition process by modifying the local propellant-supply conditions encountered by the circumferential pressure waves, while the eventual dominant propagation direction emerges progressively during this unsteady establishment process.

Because the direction-selection mechanism discussed above depends on the transient wave-competition process, a fixed-grid time-step sensitivity assessment was also

performed for this representative Case 5 condition. Calculations were carried out on the same medium grid of approximately 1.80 million cells using time steps of 6×10^{-7}, 5×10^{-7}, and 4×10^{-7} s, while keeping the computational grid and all other numerical settings unchanged. Across the analyzed early establishment interval, all three time-step settings showed the same qualitative directional tendency: CW and CCW circumferential wave systems coexisted and competed, while the CW component developed to a higher level than the CCW component. Therefore, within the examined time-step range, temporal refinement did not alter the preferential CW development identified for the transient wave-competition process.

To move beyond the qualitative pressure-field evidence in Figure 15, a quantitative directional-wave decomposition was performed for the same representative Case 5 establishment process. The circumferential pressure perturbation was extracted from an annular region near the outer wall of the head-end transverse cross-section ($r = 38.0$–41.95 mm) and defined as

$$p'(\theta, t) = p(\theta, t) - \langle p(\theta, t) \rangle_\theta. \tag{17}$$

The first circumferential Fourier mode ($m = 1$), corresponding to the final single-wave rotating-detonation mode, was then obtained from

$$a_1(t) = \left\langle p'(\theta, t) \exp(-\mathrm{i}\theta) \right\rangle_\theta. \tag{18}$$

A two-sided short-time Fourier transform (STFT) was applied to the complex coefficient $a_1(t)$ to separate the oppositely travelling components. With the present angular convention, increasing θ corresponds to the CW direction; therefore, the negative- and positive-frequency components of $a_1(t)$ correspond to CW- and CCW-propagating waves, respectively. A Hann window of 300 µs with 80% overlap was used, and the directional spectral energies were integrated over $|f| = 2.5$–12 kHz as

$$E_{\mathrm{CW}}(t) = \sum_{-f_{\max} \le f \le -f_{\min}} |Z_1(f, t)|^2, \tag{19}$$

$$E_{\mathrm{CCW}}(t) = \sum_{f_{\min} \le f \le f_{\max}} |Z_1(f, t)|^2, \tag{20}$$

where $Z_1(f, t)$ is the two-sided STFT coefficient. The directionality index (DI) is defined as

$$\mathrm{DI}(t) = \frac{E_{\mathrm{CW}} - E_{\mathrm{CCW}}}{E_{\mathrm{CW}} + E_{\mathrm{CCW}}}. \tag{21}$$

To avoid interpreting the directionality index when the circumferential-wave energy is negligible, DI is shown only when $E_{\mathrm{CW}} + E_{\mathrm{CCW}}$ exceeds 5% of its maximum value during the analyzed interval.

The CW and CCW directional energies shown in Figure 16b are normalized by the maximum value of the total directional energy ($E_{\mathrm{CW}} + E_{\mathrm{CCW}}$) during the analyzed process. Therefore, the normalized directional energy represents the relative strength of each directional wave component with respect to the maximum overall wave-competition intensity.

Figure 16a presents the full-circumference evolution of p' from the early establishment stage to stable propagation, whereas Figure 16b focuses on the directional-wave competition during the early establishment interval. Multiple transient circumferential pressure-wave structures coexist and interact during the early stage. As the directional-wave energy develops, the CW component becomes clearly stronger than the CCW component over the principal wave-competition interval, and DI is predominantly positive. The weaker transient structures subsequently decay while a dominant CW pressure-wave trajectory progressively emerges. After approximately $t = 1.4$ ms, a clear periodic circumferential

trajectory is maintained, corresponding to stable single-wave CW rotating detonation. This evolution is consistent with the transient pressure-field development shown in Figure 15.

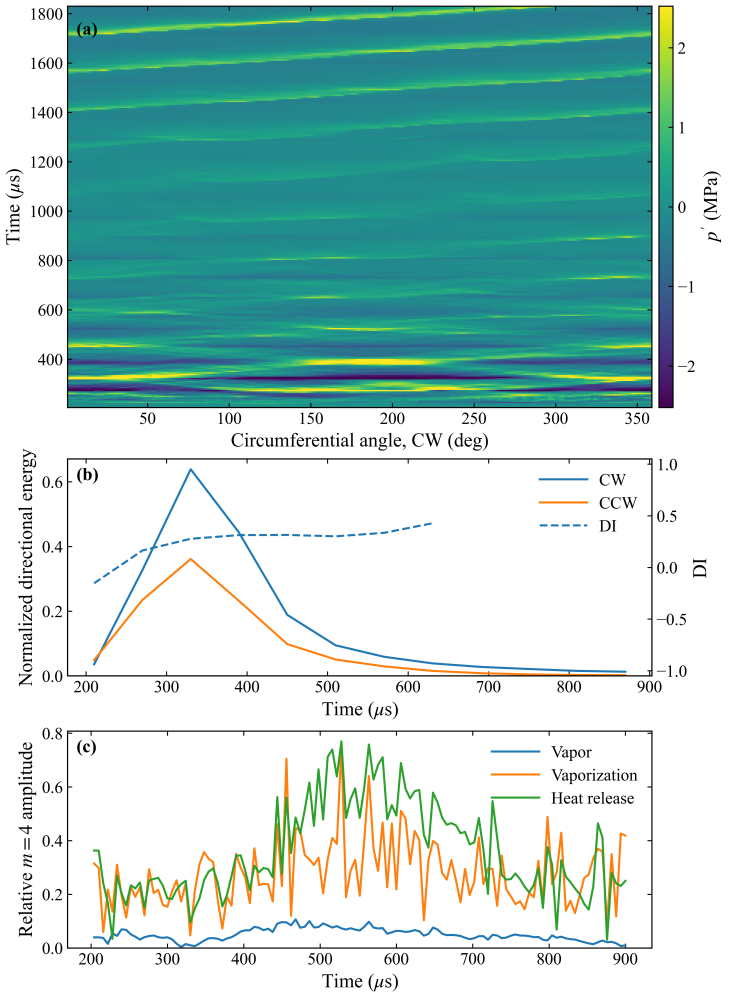


Figure 16. Quantitative characterization of wave competition and circumferential non-uniformity for Case 5: (**a**) full-circumference evolution of the pressure perturbation near the combustor outer wall from transient establishment to stable single-wave propagation; (**b**) normalized directional spectral energies of the $m = 1$ CW and CCW components and the corresponding directionality index (DI) during the early establishment stage; (**c**) relative $m = 4$ amplitudes of the vapor-phase propellant concentration, droplet-vaporization source, and heat-release field near the injector distribution circle during the early establishment stage.

To further characterize the circumferential environment responsible for this unequal wave development, the vapor-phase propellant concentration, droplet-vaporization source, and heat-release field were evaluated in an annular region surrounding the injector distribution circle ($r = 32$–38 mm). Because the S_4–M_4–L_4 arrangement contains four repeated circumferential periods, the relative amplitude of the $m = 4$ mode was used to quantify the spatial non-uniformity of a field ϕ:

$$A_{4,\phi}(t) = \frac{2|c_{4,\phi}(t)|}{|\overline{\phi}(t)|}, \qquad c_{4,\phi}(t) = \langle \phi(\theta, t) \exp(-4\mathrm{i}\theta) \rangle_\theta. \tag{22}$$

Here, the vapor quantity is the sum of the gas-phase N_2O_4 and MMH mass fractions, the vaporization quantity is the sum of the two DPM vaporization source terms, and the heat-release quantity is obtained from the local heat-of-reaction field. As shown in Figure 16c, the total vapor-phase propellant concentration exhibits only a relatively weak

$m = 4$ component, indicating substantial smoothing by circumferential transport and mixing. In contrast, the droplet-vaporization source and heat-release field retain substantially stronger $m = 4$ components during the establishment process.

Taken together, the directional-wave decomposition and the field-non-uniformity analysis support the interpretation that circumferentially non-uniform injection establishes a spatially persistent non-uniform replenishment and energy-release environment during rotating-detonation establishment. Because the CW and CCW wave systems traverse the prescribed S/M/L regions in opposite circumferential sequences, they experience different histories of local droplet vaporization, reactant replenishment, and heat release. This asymmetric environment is consistent with the observed unequal development of the two competing circumferential-wave systems and the progressive selection of the final propagation direction. The present analysis does not isolate the individual causal contribution of each local process; rather, it provides quantitative evidence linking the imposed circumferential injection non-uniformity to asymmetric wave competition during the establishment stage. Accordingly, the effect of the non-uniform injection is interpreted as acting primarily through wave competition under an asymmetric local replenishment and heat-release environment, rather than as a direct kinematic forcing of an already established rotating detonation.

4. Conclusions

This study numerically investigated how circumferentially non-uniform injection influences propagation-direction selection of MMH/NTO rotating detonation in a hollow combustor. The effects of injector-group length, non-uniformity amplitude, injection-arrangement direction, post-establishment arrangement reversal, and transient wave-system evolution were examined.

Propagation-direction selection depends on both the circumferential injector-group length and the non-uniformity amplitude. The S_1–M_1–L_1 and S_2–M_2–L_2 configurations did not exhibit a consistent directional preference in the repeated simulations. In contrast, at $\delta = 0.4$, all five simulations with the CW S_4–M_4–L_4 arrangement developed CW rotating detonation, while all five simulations with the reversed arrangement developed CCW rotating detonation. When the amplitude was increased to 0.6, propagation opposite to the injection arrangement was observed in the limited simulations performed, showing a non-monotonic directional response under the investigated conditions.

Once stable unidirectional rotating detonation was established, reversing the circumferential injection arrangement did not reverse the propagation direction. The detonation wave retained its original direction, although the dominant pressure frequency decreased from approximately 7.18 to 7.06 kHz and the local heat-release and temperature distributions changed. Circumferential redistribution of the propellant supply therefore has a stronger influence on direction selection during detonation establishment than on the propagation direction of an already established wave.

Transient pressure fields further showed that oppositely propagating circumferential pressure waves coexist and compete before stable rotating detonation is formed. Under non-uniform injection, the two wave systems encounter different sequences of local propellant replenishment and reaction environments; one wave system weakens while the other persists and is amplified into the final single-wave rotating detonation. For the hollow-combustor configuration and operating conditions considered here, these results indicate that circumferential propellant redistribution can influence the eventual propagation direction by modifying the early wave-competition process, without requiring geometric guidance or the direct introduction of tangential injection momentum.

The quantitative $m = 1$ directional-wave decomposition further shows that the CW and CCW components become unequal during the establishment stage, while the $m = 4$ analysis demonstrates that the droplet-vaporization and heat-release fields retain pronounced circumferential non-uniformity even though the total vapor-phase propellant concentration is substantially smoothed. These results provide additional quantitative support for interpreting propagation-direction selection as a progressive wave-competition process occurring within an asymmetric local replenishment and heat-release environment.

Author Contributions: Formal analysis, Y.X.; data curation, Y.X.; writing—original draft preparation, Y.X.; resources, K.G.; investigation, Y.Q. and X.L.; writing—review and editing, W.L. and Q.X.; supervision, W.L. All authors have read and agreed to the published version of the manuscript.

Funding: This research was funded by the State Key Laboratory of Advanced Space Propulsion, grant number 2025ASP0203, and the Open Fund of the Innovation Center for Space Launch Testing and TT&C Technology, grant number CXZX-25-01-04.

Institutional Review Board Statement: Not applicable.

Informed Consent Statement: Not applicable.

Data Availability Statement: The data presented in this study are available from the corresponding author upon reasonable request.

Conflicts of Interest: The authors declare no conflicts of interest.

References

1. Yun, M.S.; Roh, T.S.; Lee, H.J. Analysis of Development Trends for Rotating Detonation Engines Based on Experimental Studies. *Aerospace* **2024**, *11*, 570. [CrossRef]
2. Heister, S.D.; Smallwood, J.; Harroun, A.; Dille, K.; Martinez, A.; Ballintyn, N. Rotating Detonation Combustion for Advanced Liquid Propellant Space Engines. *Aerospace* **2022**, *9*, 581. [CrossRef]
3. Sawada, S.; Ishihara, K.; Itouyama, N.; Watanabe, H.; Kawasaki, A.; Matsuoka, K.; Kasahara, J.; Matsuo, A.; Funaki, I. The circumferential force on a cylindrical rotating detonation engine. *Proc. Combust. Inst.* **2024**, *40*, 105490. [CrossRef]
4. Sawada, S.; Goto, K.; Ishihara, K.; Kawasaki, A.; Matsuoka, K.; Kasahara, J.; Matsuo, A.; Funaki, I. Torque Around Axial Direction on Rotating Detonation Engines. *J. Propuls. Power* **2022**, *38*, 59–70. [CrossRef]
5. Goto, K.; Matsuoka, K.; Matsuyama, K.; Kawasaki, A.; Watanabe, H.; Itouyama, N.; Ishihara, K.; Buyakofu, V.; Noda, T.; Kasahara, J.; et al. Space Flight Demonstration of Rotating Detonation Engine Using Sounding Rocket S-520-31. *J. Spacecr. Rocket.* **2023**, *60*, 273–285. [CrossRef]
6. Buyakofu, V.; Matsuoka, K.; Matsuyama, K.; Kawasaki, A.; Watanabe, H.; Itouyama, N.; Goto, K.; Ishihara, K.; Noda, T.; Kasahara, J.; et al. Flight Demonstration of Pulse Detonation Engine Using Sounding Rocket S-520-31 in Space. *J. Spacecr. Rocket.* **2023**, *60*, 181–189. [CrossRef]
7. Nlcholls, J.A.; Cullen, R.E.; Ragl, K.W. Feasibility studies of a rotating detonation wave rocket motor. *J. Spacecr. Rocket.* **1966**, *3*, 893–898. [CrossRef] [PubMed]
8. Boening, J.A.; Wheeler, E.A.; Heath, J.D.; Koch, J.V.; Mattick, A.T.; Breidenthal, R.E.; Knowlen, C.; Kurosaka, M. Rotating Detonation Engine Using a Wave Generator and Controlled Mixing. *J. Propuls. Power* **2018**, *34*, 1364–1375. [CrossRef]
9. Sheng, Z.; Cheng, M.; Shen, D.; Wang, J. An active direction control method in rotating detonation combustor. *Int. J. Hydrogen Energy* **2022**, *47*, 23427–23443. [CrossRef]
10. Stoddard, W.; Gutmark, E. Numerical Study of Obstacles in Rotating Detonation Engines. In *Proceedings of the 51st AIAA Aerospace Sciences Meeting Including the New Horizons Forum and Aerospace Exposition*; American Institute of Aeronautics and Astronautics: Reston, VA, USA, 2013. [CrossRef]
11. Bach, E.; Paschereit, C.O.; Stathopoulos, P.; Bohon, M.D. Rotating Detonation Wave Direction and the Influence of Nozzle Guide Vane Inclination. *AIAA J.* **2021**, *59*, 5276–5287. [CrossRef]
12. Zhao, T.; Zhu, J.F.; Ling, M.T.; Yan, C.; You, Y.C. Coupling characteristic analysis and propagation direction control in hydrogen–air rotating detonation combustor with turbine. *Int. J. Hydrogen Energy* **2023**, *48*, 22250–22263. [CrossRef]
13. Yang, X.K.; Song, F.; Wu, Y.; Zhou, J. Experimental study of mode control in rotating detonation combustor using Tesla valve mode control configuration fueled by kerosene. *Exp. Therm. Fluid Sci.* **2024**, *151*, 111075. [CrossRef]

14. Sawada, S.; Itouyama, N.; Matsuoka, K.; Kasahara, J.; Braun, J.; Paniagua, G.; Kawasaki, A.; Higashino, K.; Matsuo, A.; Funaki, I. Direction Control of Rotating Detonation Waves with Helical Combustion Chambers. *J. Propuls. Power* **2025**, *41*, 164–177. [CrossRef]
15. Koo, I.H.; Lee, K.H.; Kim, M.S.; Han, H.S.; Kim, H.; Choi, J.Y. Effects of Injector Configuration on the Detonation Characteristics and Propulsion Performance of Rotating Detonation Engine (RDE). *Aerospace* **2023**, *10*, 949. [CrossRef]
16. Shi, L.; Fan, E.; Shen, H.; Wen, C.Y.; Shang, S.; Hu, H. Numerical Study of the Effects of Injection Conditions on Rotating Detonation Engine Propulsive Performance. *Aerospace* **2023**, *10*, 879. [CrossRef]
17. Braun, E.; Dunn, N.; Lu, F. Testing of a Continuous Detonation Wave Engine with Swirled Injection. In *Proceedings of the 48th AIAA Aerospace Sciences Meeting Including the New Horizons Forum and Aerospace Exposition*; American Institute of Aeronautics and Astronautics: Reston, VA, USA, 2010. [CrossRef]
18. Yamamoto, T.; Matsuoka, K.; Itouyama, N.; Manabe, A.; Ide, Y.; Kasahara, J.; Fujiwara, K.; Matsuo, A. Active direction control of rotating detonation waves by swirl injection. *Proc. Combust. Inst.* **2026**, *42*, 106196. [CrossRef]
19. Zhao, T.; Liu, H.; Guan, L.; Chen, H.; Yao, F.; Yu, P.; Liu, C. Research progress in combustion stability of space attitude and orbit control engines with hypergolic propellants. *J. Propuls. Technol.* **2025**, *46*, 6–24. [CrossRef]
20. Tan, Y.; Liu, X. A review of starting and ignition issues in space hypergolic propellant engines. *J. Rocket. Propuls.* **2025**, *51*, 1–16. [CrossRef]
21. Gu, F.; Cao, W.; Yu, P.; Li, Y.; Lin, W.; Guo, K.; Dou, X. Correlation mechanism between pressure oscillation characteristics of high-frequency tangential combustion instability in hypergolic propellants and rotating detonation. *Acta Astronaut.* **2026**, *239*, 535–545. [CrossRef]
22. Gu, F.; Yao, Y.; Guo, K.; Cao, W.; Yu, P.; Lin, W.; Tong, Y. Experimental and numerical analysis of rotating detonation in liquid hypergolic propellants. *Phys. Fluids* **2025**, *37*, 103312. [CrossRef]
23. Gu, F.; Cao, W.; Guo, K.; Tong, Y.; Lin, W.; Jiang, H.; Xiong, Y. Numerical simulation of rotating detonation flow field using hypergolic propellants. *J. Propuls. Technol.* **2025**, *46*, 304–313. [CrossRef]
24. Xue, S.; Liu, H.; Zhou, L.; Yang, W.; Hu, H.; Yan, Y. Experimental research on rotating detonation with liquid hypergolic propellants. *Chin. J. Aeronaut.* **2018**, *31*, 2199–2205. [CrossRef]
25. Yan, Y.; Wang, Z.; Yang, B.; Hu, H.; Hong, L. Experimental research on the detonation behavior in annular combustors utilizing liquid hypergolic propellants. *Acta Astronaut.* **2023**, *211*, 865–876. [CrossRef]
26. Yan, Y.; Hu, H.B.; Hong, L.; Yang, A.L.; Chen, F. Experimental Investigation on Rotated Detonation Combustion of Hypergolic Propellants. *Tuijin Jishu/J. Propuls. Technol.* **2018**, *39*, 1986–1993. [CrossRef]
27. Yan, Y.; Wang, Z.; Hu, H. Unsteady rotating detonation phenomenon of hypergolic propellant in annular combustor. *J. Rocket. Propuls.* **2023**, *46*, 55–62+81.
28. Nair, A.P.; Keller, A.R.; Lima, A.B.; Spearrin, R.M. Deflagration-to-detonation transition in an annular combustor with hypergolic propellants. In Proceedings of the AIAA SciTech Forum and Exposition, San Diego, CA, USA, 3–7 January 2022.
29. Nair, A.P.; Keller, A.R.; Minesi, N.Q.; Pineda, D.I.; Spearrin, R.M. Detonation cell size of liquid hypergolic propellants: Estimation from a non-premixed combustor. *Proc. Combust. Inst.* **2023**, *39*, 2757–2765. [CrossRef]
30. Nair, A.P.; Keller, A.R.; Morrow, D.S.; Lima, A.B.; Spearrin, R.M.; Pineda, D.I. Hypergolic Continuous Detonation with Space-Storable Propellants and Additively Manufactured Injector Design. *J. Spacecr. Rocket.* **2022**, *59*, 1332–1341. Correction in *J. Spacecr. Rocket.* **2023**, *60*, 3. https://doi.org/10.2514/1.A35272.c1. [CrossRef]
31. Keller, A.R.; Nair, A.P.; Kuenning, N.; Minesi, N.; Spearrin, R.M. Annular chamber geometry effects on a hypergolic liquid rotating detonation rocket engine. In *Proceedings of the AIAA Aviation and Aeronautics Forum and Exposition, AIAA AVIATION Forum 2023, San Diego, CA, USA, 12–16 June 2023*; American Institute of Aeronautics and Astronautics Inc., AIAA: Reston, VA, USA, 2023. [CrossRef]
32. Qin, X.; Yang, Q.; Wang, H.; Xu, X.; Haidn, O. Research progress in rotating detonation propulsion technology. *Acta Astronaut.* **2025**, *236*, 522–546. [CrossRef]
33. Lin, W.; Zhou, J.; Liu, S.; Lin, Z. An experimental study on CH4/O2 continuously rotating detonation wave in a hollow combustion chamber. *Exp. Therm. Fluid Sci.* **2015**, *62*, 122–130. [CrossRef]
34. Tang, X.M.; Wang, J.P.; Shao, Y.T. Three-dimensional numerical investigations of the rotating detonation engine with a hollow combustor. *Combust. Flame* **2015**, *162*, 997–1008. [CrossRef]
35. Yoneyama, K.; Ishihara, K.; Ito, S.; Watanabe, H.; Itouyama, N.; Kawasaki, A.; Matsuoka, K.; Kasahara, J.; Matsuo, A.; Funaki, I. Experimental Clarification on Detonation Phenomena of Liquid Ethanol Rotating Detonation Combustor. In *Proceedings of the AIAA SCITECH 2022 Forum*; American Institute of Aeronautics and Astronautics: Reston, VA, USA, 2022. [CrossRef]
36. Xue, S.; Ying, Z.; Ma, H.; Zhou, C. Experimental Investigation on Two-Phase Rotating Detonation Fueled by Kerosene in a Hollow Directed Combustor. *Front. Energy Res.* **2022**, *10*, 951177. [CrossRef]

37. Ishihara, K.; Sato, T.; Kimura, T.; Nakajima, K.; Nakata, K.; Itouyama, N.; Kawasaki, A.; Matsuoka, K.; Matsuyama, K.; Kasahara, J.; et al. Nitrous Oxide/Ethanol Cylindrical Rotating Detonation Engine for Sounding Rocket Space Flight. *J. Spacecr. Rocket.* **2025**, *62*, 44–54. [CrossRef]
38. Pritschau, T.; Karnam, A.; Gutmark, E. Characterizing acoustic modes in a hollow rotating detonation combustor. *Combust. Flame* **2025**, *275*, 114057. [CrossRef]
39. Fan, L.; Guo, K.; Shu, C.; Chen, P.; Nie, W.; Lin, W. Stability analysis of continuous rotating detonation in hollow combustor. *Hangkong Dongli Xuebao/J. Aerosp. Power* **2023**, *38*, 1090–1101. [CrossRef]
40. Xiong, Y.; Lin, W. Numerical Investigation on Flow Field Structures of Rotating Detonation with Hypergolic Propellants in an Annular Combustion Chamber. In Proceedings of the 3rd Aerospace Frontier Conference, Nanjing, China, 10–13 April 2026.
41. Xiong, Y.; Lin, W. Numerical Investigation on the Effect of Nozzle on Flow-Field Structures in a Hollow Rotating Detonation Combustor Fueled by Hypergolic Propellants. In Proceedings of the 3rd Chinese Conference of Aerodynamics, Shenyang, China, 2–5 July 2026.
42. Xiong, Y.; Zhao, Z. Weakly Self-Sustained Propagation Characteristics of Rotating Detonation with Hypergolic Propellants in a Hollow Combustor. *Acta Aerodyn. Sin.* 2026, *accepted*.
43. Xiong, Y.; Lin, W. Numerical Investigation of the Effects of Oxygen-to-Fuel Ratio on Rotating Detonation Characteristics of Hypergolic Propellants in a Hollow Combustor. *J. Aerosp. Power* 2026, *submitted*.
44. Sung, B.K.; Kasahara, J.; Choi, J.Y. Numerical investigation on the detonative tangential combustion instability in a rocket combustor. *Combust. Flame* **2025**, *275*, 114092. [CrossRef]
45. Guo, K.; Xu, B.; Ren, Y.; Tong, Y.; Nie, W. Analysis of Tangential Combustion Instability Modes in a LOX/Kerosene Liquid Rocket Engine Based on OpenFOAM. *Front. Energy Res.* **2022**, *9*, 810439. [CrossRef]

Disclaimer/Publisher's Note: The statements, opinions and data contained in all publications are solely those of the individual author(s) and contributor(s) and not of MDPI and/or the editor(s). MDPI and/or the editor(s) disclaim responsibility for any injury to people or property resulting from any ideas, methods, instructions or products referred to in the content.